Bachelor`s project

NTNU
Norwegian University of Science and Technology
Faculty of Engineering
Department of Energy and Process Engineering

Omar Shagouri

Testing Lithium-ion batteries thermal conductivity

The effect of electrolyte, external pressure, ageing and thermal interface resistance on the thermal conductivity of Lithium-ion battery.

Bachelor's Project in Renewable Energy (Fornybar energi)
Supervisor: Odne Burheim and Lena Spitthoff (NTNU)
May 2021

NTNU
Norwegian University of Science and Technology

NTNU | Norwegian University of Science and Technology

Bachelor Thesis

Project Title: The effect of electrolyte, external pressure, ageing and thermal interface resistance on the thermal conductivity of Lithium-ion battery.	**Given Date:** 05.01.2021 **Deadline:** 20.05.2021 **Pages/Appendix:** 37/7
Study Program: Engineering Renewable Energy	
Author: Omar Shagouri	
Supervisors: Odne Burheim Lena Spitthoff	

Available	√
Available by agreement with employer	
The report is released after	

Preface

The thesis is written by Omar Shagouri as the finishing part of Bachelor of Science degree program in Renewable Energy at the Department of Energy and Process Engineering (EPT), Norwegian University of Science and Technology (NTNU). All the measurements and experiments that have been performed in this thesis are done in the Lithium ion battery lab at NTNU-Trondheim in collaboration with Ph.D. candidate Lena Spitthoff.

Today's massive demand for Lithium ion battery motivates researchers worldwide to improve the current Lithium ion battery and its operating conditions. Increasing the cell capacity, power density, and charging rate will generate a massive amount of heat inside the cell. Therefore, the thermal management of batteries is very important. Accurate prediction of temperature values inside the battery will help to improve the thermal management system. The battery cell components thermal conductivity are key parameters of the temperature distribution inside the battery. My motivation for this thesis is to increase the understanding of the factors that affect the thermal conductivity values for lithium ion battery components.

I would like to express sincere gratitude to my internal supervisors at NTNU, Odne Burheim, for giving me the opportunity to perform this project at the NTNU lab, and to Lena Spitthoff, for assisting with weekly guidance during the project period and the feedback during the writing of the thesis.

Trondheim, May 2021

Omar Shagouri

Abstract

Heat generation and cell internal temperature have a large impact on Lithium-ion battery (LIB) cell performance and ageing mechanisms. Therefore, the battery thermal management system plays a critical role in mitigating all these effects during the battery life cycle. Understanding the thermal conductivities of the battery components and the factors that affect these values will help predict the temperature inside the cell, further improve the thermal management system.

This thesis reports the thermal conductivity of an FS3006-25 separator and commercial electrodes from two LIB cells. One cell utilizing LCO as the cathode and graphite as the anode, the other cell utilizing an NMC cathode and graphite anode. The materials are measured at different compaction pressure steps. In addition, the effect of the electrolyte solvent, cell assembly and thermal interface resistance between the cell layers were investigated. Finally, the effect of these factors on the heat transport inside the battery was determined using a simple one-dimensional thermal model simulating the temperature distribution inside the battery.

The thermal conductivity of the separator ranged from 0.116 to 0.124 $Wk^{-1}m^{-1}$ for an applied pressure from 2.7 to 11.6 bar. NMC cathode thermal conductivity ranged from 0.35 to 0.38 $Wk^{-1}m^{-1}$ while the LCO cathode ranged from 0.51 to 0.65 $Wk^{-1}m^{-1}$. In the case of anodes, the thermal conductivity ranged from 0.427 to 0.597 $Wk^{-1}m^{-1}$. Adding the electrolyte solvent increased the thermal conductivity of the measured materials by a factor of 2 to 4.

In addition, the thermal models showed that adding the electrolyte to the cell layers decreases the centre temperature by 0.8 K for the NMC cell (30 A/m^2 charging current density), while the LCO cell (13.1 A/m^2 charging current density) centre temperature decreased by 0.08 K. Furthermore, electrodes at beginning of life (BOL) thermal conductivity are measured and compared to fresh electrodes. The BOL NMC cathode measurement showed around 35 % lower thermal conductivity values compering to the fresh cathode.

Finally, the thermal interface resistance between the LIB cell layers is measured. Results showed a thermal contact resistance of 4.3 E-5 Km^2w^{-1} for the LCO cathode and 2.1 E-5 Km^2w^{-1} for the NMC cathode. Anode thermal contact resistance to the separator is measured at about 6.5 E-5 Km^2w^{-1}. Adding the electrolyte solvent decreased the thermal contact resistance by a factor of about 2 for the cathodes and about 7 for the anode.

Summary (Norwegian)

Varmeproduksjon og batteriets indre temperatur har stor innvirkning på ytelse og aldring av litium-ion batteri (LIB). Derfor spiller batteriets termiske styringssystem en avgjørende rolle for å redusere disse effektene i løpet av batteriets levetid. Å forstå de termiske ledningsevnene til batterikomponentene og de faktorene som påvirker disse evnene, vil bidra til mer nøyaktig temperaturforutsigelse inne i cellen og vil bidra til å forbedre strategiene for termisk styring i disse batterier.

Denne oppgaven rapporterer termisk ledningsevne til en FS3006-25 separator og kommersielle elektroder fra to LIB-celler. En celle som bruker LCO som katode og grafittanode, den andre cellen bruker en NMC katode og grafittanode. Materialene har målt under forskjellige trinn av komprimeringstrykk. I tillegg ble effekten av elektrolyttløsningsmidlet, celle aldring og termisk grensesnittmotstand mellom cellelagene undersøkt. Til slutt ble effekten av disse faktorene på den termiske varmetransporten inne i batteriet bestemt ved hjelp av en enkel endimensjonal termisk modell som simulerte temperaturfordelingen inne i batteriet.

Separatorens varmeledningsevne varierte fra 0.116 til 0.124 $Wk^{-1}m^{-1}$ for et påført trykk fra 2,7 til 11,6 bar. NMC-katodens varmeledningsevne varierte fra 0,35 til 0,38 $Wk^{-1}m^{-1}$ mens LCO-katoden varierte fra 0,51 til 0,65 $Wk^{-1}m^{-1}$. Når det gjelder anoder, varierte varmeledningsevnen fra 0,427 til 0,597 $Wk^{-1}m^{-1}$. Tilsetning av elektrolyttløsningsmidlet økte materialers varmeledningsevne med en faktor på 2, 3 og 4.

De termiske modellene viste at tilsetning av elektrolyttløsningsmidlet tilLIB-cellelagene senker temperaturen i senteren av batteriet med 0,8 K for den NMC cellen (30 A/m^2 current density), mens den LCO (13,1 A/m^2 current density) temperaturen i senteren av batteriet redusert med 0,08 K. Videre, elektroder fra batteriet ved (beginning of life BOL) varmeledningsevne har målet og sammenlignet med friske elektroder (aldri vært i batteri før). BOL NMC katode måling viste rundt 35 % lavere varmeledningsevneverdier enn friske katoden

Til slutt, den termisk kontaktmotstand mellom LIB-cellelagene ble målet. Resultatene viste en termiske kontaktmotstand på 4,3 E-5 Km^2w^{-1} for LCO-katoden og 2,1 E-5Km^2w^{-1} for NMC-katoden. Anodenes termisk kontaktmotstand mot separatoren har målet på omtrent 6.5 E-5 Km^2w^{-1}. Tilsetning av elektrolyttløsningsmidlet reduserte termisk kontaktmotstand med en faktor på ca. 2 for katodene og ca. 7 for anodene.

Contents

List of Symbols

k	Thermal conductivity $Wk^{-1}m^{-1}$
A	Battery surface area m2
F	Faraday constant (96485) A·s/mo
Q	Heat flux W/m2
ΔS	Entropy change J/(mol·K)
P	Pressure bar
H	Enthalpy change J/mol
T	Temperature K
j	Current density $Am^{-}2$

List of Abbreviations

LIB	Lithium Ion Battery.
Li^{+}	lithium-ions.
LCO	Lithium Cobalt Oxyde $LiCoO_2$.
NMC	Nickel Manganese Cobalt
NCA	Nickel Cobalt Aluminum
C-rate	The rate at which a battery is being charged/discharged.
BTMS	Battery Thermal Management System
LFP	Lithium iron phosphate
SEI	Solid electrolyte interphase
BOL	Beginning of life
EOL	End of life
EC	Ethylene carbonate
DMC	Dimethyl carbonate
DEC	Diethyl carbonate
PC	Propylene carbonate
1D	One dimensional
TDMS	Test Data Migration Server

List of Figures

List of Tables

1 Introduction

This section explains the background and introduces the problem statement for the thesis. Further, it describes the motivation, scope and outline of this thesis.

1.1 Background

Due to its durability, high specific energy (140 to 200 Wh/kg) [1], and the ability to operate at reasonably high power, Lithium ion batteries (LIB) are currently the most used battery technology for portable devices, including cell phones, laptop computers and power tools [2]. Recently, LIB has been chosen by the automotive sector as power packs for electric and hybrid vehicles. As larger battery cells have become cheaper, LIB have been introduced to larger scale electric and hybrid electric vehicles, like electric buses, trucks and ships [3].

In addition to the automotive sector, LIB batteries gradually enter the stationary service implementing uncontrollable renewable energy technology such as wind and solar energy. That makes the demand for LIB and production of these batteries increase expeditiously [2].

1.2 Motivation

The massive demand for batteries by the automotive market and all other applications motivates researchers worldwide to improve the current LIB and its operating conditions. Increasing cell capacity, power density, and charging rate lead to large amounts of heat generation inside the cell. Heat generation and cell internal temperature have a large impact on cell performance and ageing mechanisms [4]. Therefore battery thermal management system plays a critical role in mitigating all these effects during the battery life cycle [5]. Accurate prediction of temperature values inside the battery will help to improve the thermal management system. The thermal conductivities of the battery components are key parameters for this temperature prediction and distribution inside the battery [6].

Thermal conductivity and the internal temperature distribution for several LIB materials reported in the literature e.g. [6–10]. Using an in-situ measurement setup(Rig), the thermal conductivity measured for all the cell components; from these values, the battery thermal conductivity has been calculated. In the literature, when the through-plane thermal conductivity of a full battery was calculated from the thermal conductivity of the single layers, the thermal interface resistance has been neglected, assuming that will not affect the thermal conductivity values [7]. Developing a method to measure this resistance inside the LIB cells and investigating its affect on the thermal conductivity and the temperature distribution inside the battery will answer if that is fair or not.

Furthermore, applying different compaction pressures on the samples during the measurements will give an understanding of how the pressure affects the cell components thermal conductivity. Moreover, measuring the cell layers dry and soaked in electrolyte solvent determines the electrolyte impact on thermal conductivity. Finally, comparing the thermal conductivity values at two different phases of ageing will give an understanding how the battery's ageing will affect the thermal behaviour inside the battery.

1.3 Scope of this thesis

In this thesis, the thermal conductivities of electrodes of two different LIB were measured. One cell (Melasta cell) utilizing LCO as the cathode and graphite as the anode, the other cell (Custom cell) utilizing a NMC cathode and graphite anode. The materials were measured at different conditions simulating the conditions inside the battery. The thermal conductivity measured at pressure steps in a range of 2.7 to 11.6 bar. Further, the impact of the electrolyte on the thermal conductivity will be investigated by measuring the material dry and soaked in electrolyte solvent for both cells. Moreover, the thermal conductivity at two different phases av ageing for the Custom cell layers measured and compared. The thermal interface resistance between the cell layers is calculated and its effect on the effective thermal conductivity on the cell is estimated. Finally, temperature profiles are estimated for different material conditions and pressure steps using a 1 D, steady-state thermal-model.

1.4 Thesis Outline

Section 1 introduces the problem statement and the motivation and aim of this thesis.

Section 2 describe principles and working concept for LIB. It presents common battery materials and LIB thermal properties. Further, a brief description of thermal models and heat generation inside the battery is added to this section.

Section 3 provides a description of the measurement rig working principle and all the equations used during the calculation of the thermal conductivity. This section ends with detailed description of the method used to determine the thermal interface resistance between the LIB cell layers.

Section 4 presents and discusses all the measured and calculated results.

Section 5 provides a conclusion for the results and recommendation for further research.

2 Theory

This Section describes the working concept of LIB and introduces common used materials for cathode, anode and separator. Further, the thermal properties of LIB were described. This section ends with a brief description of battery thermal models and the heat sources inside the battery.

2.1 Lithium ion battery

2.1.1 Physical construction

LIB is built up as group of unit cells, each single unit cell has three layers anode, cathode, and separator. The anode and cathode's active material are coated into a foil of copper for the anode and aluminum for the cathode, the foil acts as a current collector here. The positive and the negative tabs are taken out from the current collectors, the anode as the negative electrode and the cathode as the positive. For larger practical battery, the current collector usually has active material on both sides.[11].

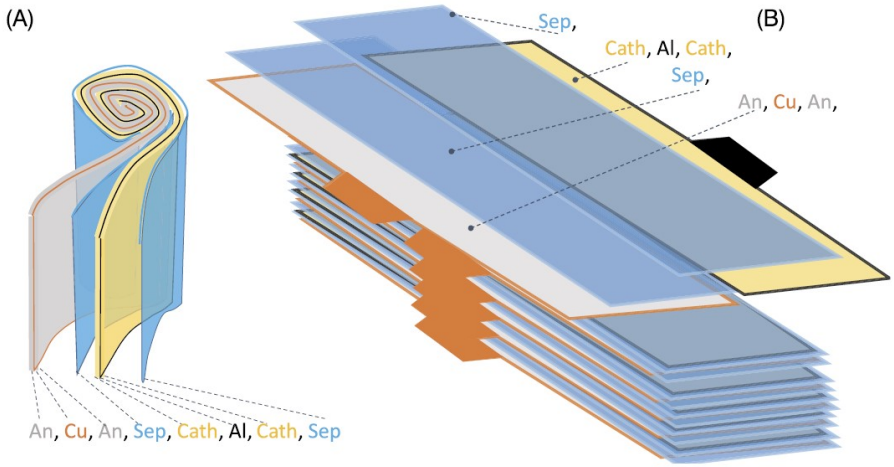

Figure 2.1: (A) Assembly principal for a cylindrical LIB. (B) Assembly principal for for a pouch LIB [11].

Two common ways of assembling the cell layers in a LIB are shown in figure 2.1. The first way is to stack layers as flat sheets, as showing in section (B), which gives a pouch cell battery. The second way is to form two long rectangular sheets of each electrode and the separator and roll them up, as showing in section (A), which gives a cylinder-formed battery [11].

2.1.2 Working principles

The working principle behind LIB is a recurring transmission of lithium-ions (Li^+) between the cathode and the anode. During charging, an electric field from an external circuit (charging

source) enforces Li^+ ions to be transferred from the positive electrode (cathode) through the electrolyte into the negative electrode (anode). See the red arrows on the right-hand figure 2.2. At the same time, through the external circuit, the electrons flow from the positive electrode and into the negative electrode. Back, the Li-ions and electrons flow from the negative electrode to the positive electrode during discharge [12]. This flow drives a current through an external circuit performing work [2]. The left-hand figure 2.2 shows the discharge process.

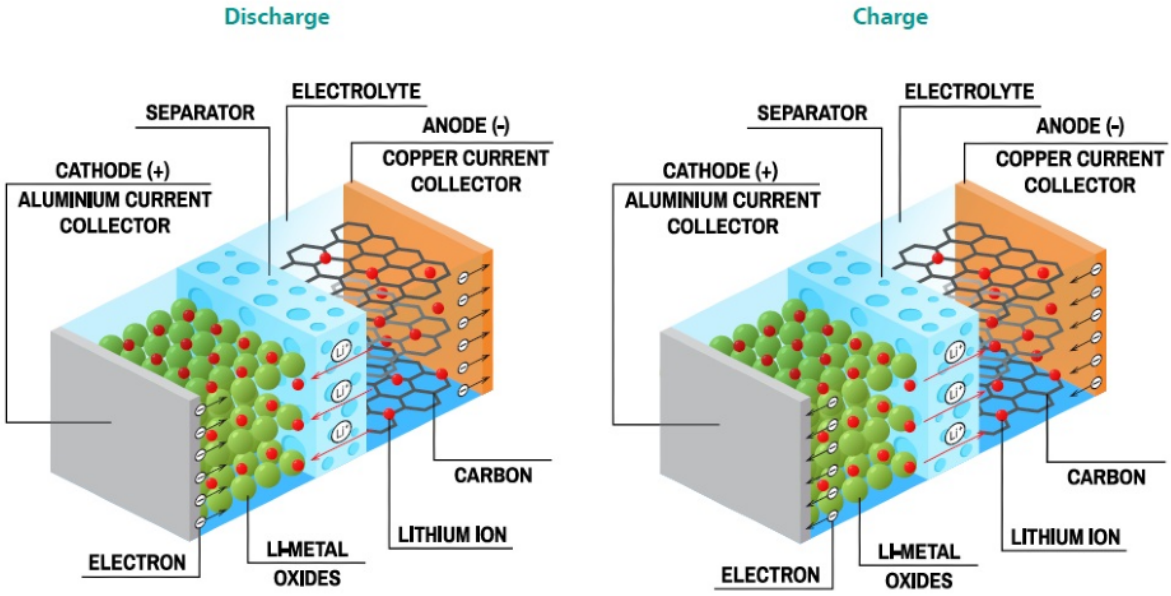

Figure 2.2: The working mechanism in LIB during charging and discharging [13].

During the first charge of the LIB, the organic electrolyte undergoes reduction at the anode. That forms a passive layer called solid electrolyte interphase (SEI). This layer mostly prevents the further reduction of the electrolyte by blocking the electrons to pass through it while allowing the pass of lithium ions during cycling [14].

2.2 Common battery materials

2.2.1 Cathode and Anode

LIB cathode has three classes of material categorized by structure: layered compounds, spinel compounds, and olivine compounds. Sony in the early 1990s, developed the first layered oxide cathode material known as Lithium cobalt oxide $LiCoO_2$ (LCO). Other common layered oxide cathodes are lithium iron phosphate (LFP), nickel-cobalt-aluminum (NCA) and nickel-manganese-cobalt (NMC) [15].

Typically the anode material is based on a form of carbon particles (e.g., graphite and hard carbon), which known for their stability, high specific capacity and less costly [15]. New anode material is utilizing silicon or titania, but they are not widely used today [11].

2.2.2 Separator and Electrolyte

The separator is often made of porous organic, polymeric or fiber glass material. Typically the thickness of a separator layer is around 20 μm . The separator layer hinders the contact between the cathode and the cathode active material and interrupts electric current short-circuiting [11].

The electrolyte generally contains a mix of organic solvents, salts and additives. The salts are the passage for Li-ions to move and a lithium-ions source inside the battery, common used salt is lithium hexafluorophosphate ($LiPF_6$) [16]. The solvents are used to dissolve the salts. Common electrolyte are ethylene carbonate (EC), dimethyl carbonate (DMC), diethyl carbonate (DEC) and propylene carbonate (PC).[2]

2.3 Thermal conductivity

2.3.1 Fourier's law

Materials have different capabilities to conduct heat; some materials like metals can conduct heat more efficiently than others (e.g wood). That depends on the physical structure of matter, atomic and molecular. The thermal conductivity K of a material is a physical property that refers to the rate at which heat is conducted. Thermal conductivity measure in $Wk^{-1}m^{-1}$. Higher conductivity means a high ability to transfer heat. Materials with low thermal conductivity are known as thermal insulators and often used to insulate houses because they reduce heat transfer [17].

Thermal conductivity for solid materials can be defined by Fourier's law. Figure 2.3 shows how the heat conducts inside a material from high temperature T_1 to lower temperature in the x-direction. For an area A from the material, Fourier's law describes the amount of heat energy transported per time unit, as shown in equation 2.1. Where A is the area of the surface measured in $[m^2]$, δT is temperature difference over distance δx measured in Kelvin, q_x is the amount heat conducted, and K is the thermal conductivity. The negative sign shows that heat moves from higher temperature regions to lower temperature regions [18].

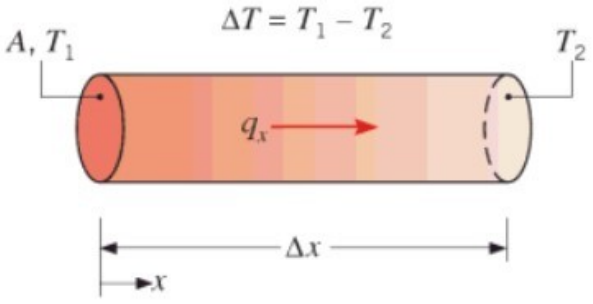

Figure 2.3: Heat conduction rate inside materials [18].

$$q_x = -kA\frac{\delta T}{\delta x} \tag{2.1}$$

The heat flux q''_x can be calculated by dividing the conduction rate q by the area A. Equation 2.2 shows the heat flux in x-direction.

$$q''_x = -k\frac{\delta T}{\delta x} \tag{2.2}$$

From equation 2.2 the thermal conductivity of a material with flux q'' in x direction can be calculated. This is shown in equation 2.3. K is measured in $(Wk^{-1}m^{-1})$ [18].

$$k = -\frac{q''_x}{(\delta T/\delta x)} \tag{2.3}$$

2.3.2 Constant heat flux

Experimentally determination of thermal conductivity following Fourier's law requires knowing or measuring the three variables δT, δx and q''_x from equation 2.3. δT and q''_x are determined by conduct one-dimensional heat flux through a sample and measure the temperature drop across it. Moreover, the thickness changes δx can be measured using micrometres. With this, the thermal conductivity can be calculated. This method is called the constant heat flux method [19].

2.4 Thermal models

Thermal model are designed to determine the temperature distribution inside the battery by mathematically simulating its thermal behaviour. Usually, a thermal model simulates the temperature distribution over a series of charge and discharge C-rate.

There are two main thermal models categories. The first category connects the thermal model to the electrical model based on an equivalent circuit or an electrochemical model. In the second category, the thermal model is based on solving the energy balance and heat generation in the battery [20].

A non-uniform temperature distribution leads to inhomogeneous and accelerated degradation. As the temperature inside a battery cell is difficult to measure, the temperature is often measured on or near the cell tabs. However, the accuracy of predicting the cell temperature with those quantities is limited. Therefore a thermal model of the battery is used in order to calculate and estimate the cell temperature. Thermal conductivity values from all cell components determine how the heat will be transferred inside the battery. Thermal model input parameters describe the different conditions and geometries for the battery [6].

2.4.1 Internal heat production

LIB convert chemical energy into electrical work with high efficiencies of about 85-90%.[21]. But even with this high efficiency, there are energy losses in form of heat. There are three main sources for heat production in LIB related to the electrochemical cell: Ohmic heating Q_{ohmic}, Tafel heating $Q_{overpotential}$ and battery reaction entropic heat $Q_{entroppic}$. All of these sources depend on the current density [8].

$$q_{Cell} = q_{ohmic} + q_{overpotential} + q_{entroppic} \tag{2.4}$$

- Ohmic heat is generated between the electrode surface. The ohmic heat can be calculated from $r_w j^2$, where r_w is the ohmic resistance and j is the current density.[22]
- The second source is related to the reduction in the cell potential. This source calculates from ηj. where η is the overpotential [23].
- The third heat source is generated from the change of entropy for the cell reaction. This heat source is reversible. It acts as a heat sink during charging and as a heat source during discharge. This heat source can be calculated from $\frac{T.\Delta S}{F} j$. F is Faraday constant, j is current density,ΔS is entropy change, and T is the temperature [24].

Equation 2.5 gives the total heat generation for LIB from these three sources during charging and equation 2.6 during discharging.

$$q_{ch} = \frac{T.\Delta S}{F} j + r_w.j^2 + \eta j \tag{2.5}$$

$$q_{disch} = -\frac{T.\Delta S}{F} j + r_w.j^2 + \eta j \tag{2.6}$$

2.4.2 1-Dimensional modeling of the internal temperature profile

This section introduces a simple thermal model based on the 1 D stationary solution of the energy balance, including the heat generated inside the battery and the heat transfer to the ambient. The model is described by Spitthoff et al. [4]. Equation 2.7 gives the 1D stationary energy balance, where δT is the internal temperature gradient, K_x is the thermal conductivity in through-plane direction, and Q is the volumetric heat production.

$$0 = \frac{\delta}{\delta_x} \left(K_x \frac{\delta T}{\delta_x} \right) + Q \tag{2.7}$$

The effective thermal conductivity in through-plane direction is calculated by normalising the thermal conductivities of the electrodes and separator by their thickness d_i, where d_{total} is the entire thickness of the battery. See equation 2.8,

$$k_{eff} = \frac{d_{total}}{\Sigma \frac{d_i}{k_i}} \tag{2.8}$$

The volumetric heat production Q_{eff} for n numbers of unit cells is calculated for one half of a full battery using equation 2.9. Where q_cell is the heat generation inside the cell (see equation2.4.1) and n is the number of the cells inside the battery.

$$Q_{eff} = \frac{q_{cell}}{d_{total}} . \frac{n}{2} \tag{2.9}$$

The temperature in the center of the battery is assumed to be the maximum temperature inside the battery. For simplification, the temperature of one half of the cell is modelled, and the center of the battery is set at x = 0. The boundary conditions are stated in 2.10. Where T_{amb} is the ambient temperature, T_{max} is the maximum temperature in the battery cell center and h is the heat transfer coefficient describes the external heat transfer. The distance from the cell centre (x=0) to the battery cell surface is $d_{total}/2$.

$$\frac{dT}{d_x}|_{x=0} = 0, T(x = d_{total}/2) = \frac{q}{h} + T_{amb} \tag{2.10}$$

3 Method

The method section presents the methodology and the parameter used in this project in order to produce valuable and correct results.

3.1 Measuring the thermal conductivity

The thermal conductivities have been measured using the thermal conductivity measurement apparatus (Rig) shown in the figure 3.1. A full description of the methodology and the apparatus described in details by Burheim et al. [19]. This apparatus uses a constant heat flux method (described in section 2.3.2) to determine thermal conductivity.

The material sample is placed between two cylinders at the center of the apparatus. The cylinders are made from steel with a 21 mm diameter. The upper cylinder is attached to heating water at 35°C, and the lower cylinder to cooling water at 10°C. The tip of each cylinder which it is in contact with the sample, is covered with a thin aluminum section. The reason for choosing aluminum is the relatively high thermal conductivity compared to steel conductivity. This creates an isothermal region adjacent to the sample [19].

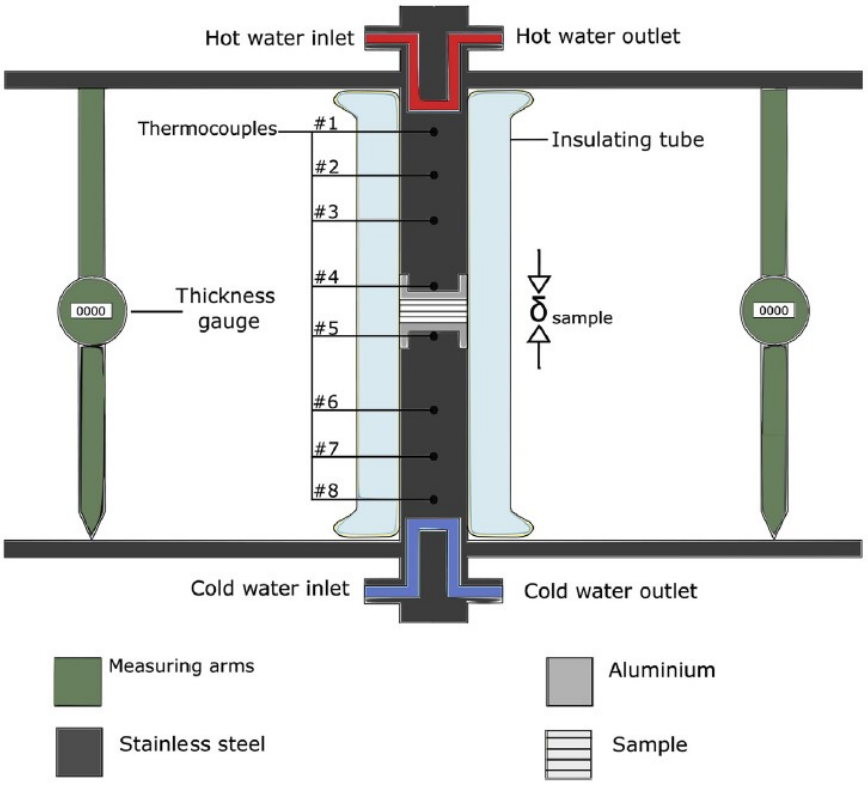

Figure 3.1: The thermal conductivity meter apparatus. The numbers 1-8 indicate the placement of the thermocouples [7].

Four thermocouples (type k) are connected to the body of each cylinder. The thermocouples measure the temperature drop from 1 to 3 and from 6 to 8 on the cylinder's body, as seen in figure 3.1. By using these temperatures, two heat flux values can be calculated. One through the upper cylinder and the other through the lower cylinder. Comparing these two values will

ensure that the heat is flowing in one direction. A tube of isolation is added around the cylinders to reduce the heat loss. Two extra thermocouples are connected to the aluminum section at 4 and 5 to measure the temperature drop across the sample [19].

Two micrometers (type Mitutoyo Digimatic Indicator ID-C Series 543) are attached to the apparatus's upper part on both sides of the cylinders. These micrometers measure the changing of sample thickness as a function of the applied pressure. A pneumatic piston is attached to the lower part of the apparatus to apply the commanded pressure. The pressure controlled by using pressure regulator (type Rexroth R434000457) [19].

Thermometers, micrometers, and pressures controller are connected to a computer. A LabView program was used to record temperature and sample thickness for all applied pressure steps. The user interface from the program showing in figure 3.2.

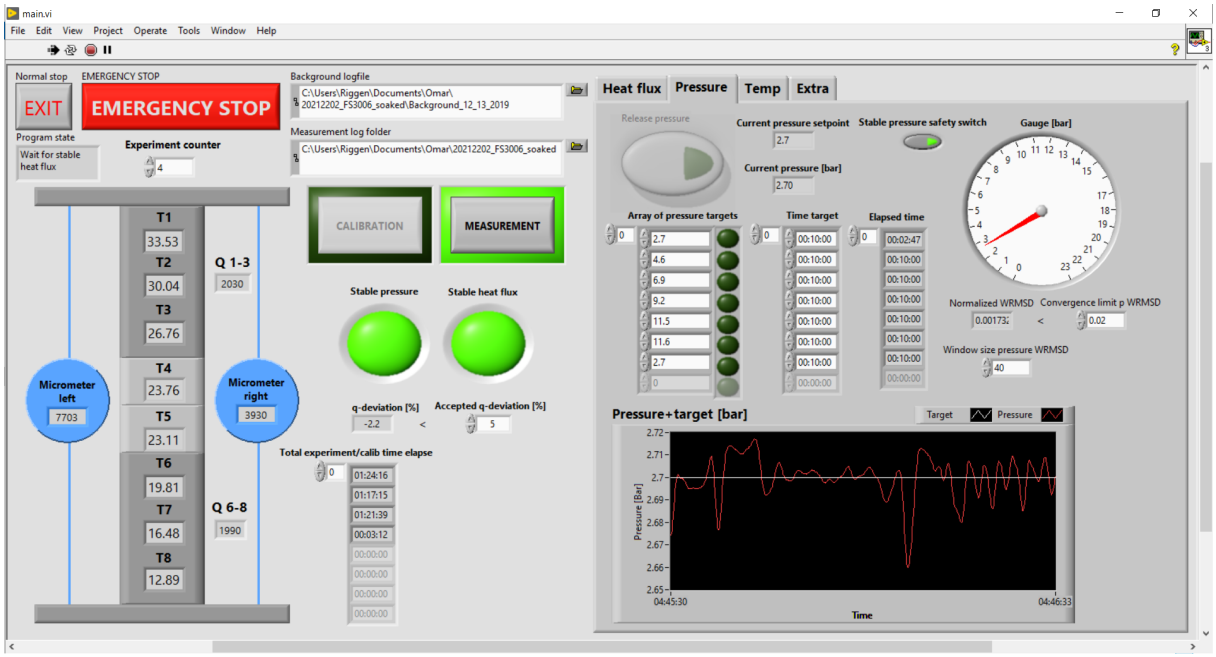

Figure 3.2: The user interface from the LabView program [7].

LabView recording measured values every second to a TDMS file, which was used for calculation. The left section on figure 3.2 shows the values measured from the thermocouples and micrometres. The right section of the interface contains the pressure window where the inputs form for the applied pressure and time steps are written. The current pressure is shown on the upright corner. The middle section shows the file directory and the test type.

The measurement is done starting with calibration without the sample; then the sample tested for three or four different thicknesses; the measurement ends with a calibration as well.

3.2 Measured materials

The first battery cell investigated in this study is the Melasta No.: SLPBB042126 from Shenzhen Melasta Battery Co. The cathode materials for this cell is based on LiCoO2. Manufacturer technical data sheet with specifications for the cell added to appendix B. The Melasta cell is the battery used in the NTNU electric race car Revolve [25]. The other cell called Custom cell utilizing a NMC cathode and graphite anode. The separator that used in this study is FS3006-25 from Viledon manufacturer.

In order to reach the aim of this project, samples from both Custom and Melasta cells measured at different conditions. The fresh materials were received from the manufacturer directly. The electrodes that are refered to as BOL electrodes were extracted from a battery cell at the beginning of life phase. This means the electrodes have been assembled to a full battery cell, undergone formation cycling at the battery producer and been stored before the electrodes have been extracted for thermal conductivity measurements. An overview of the conditions of the measured materials is added in table 3.1.

Tabell 3.1: Measured material conditions.

Material	Fresh		BOL	
	Dry	Wetted	Dry	Wetted
Fs3006-25	x	x		
CC Aanode	x		x	x
CC Cathode	x		x	x
ML Anode			x	x
ML Cathode			x	x

CC = Custom Cell

ML = Melasta Cell

3.2.1 Extracting electrodes from battery cell

As a part of this project a new Custom cell was opened to extract electrodes for the thermal conductivity measurement. The Melasta cell was opened earlier by Christian Trandem as part of his master project work [26]. The opening of the battery cell was done after fully discharging the battery. The cell was opened inside a glove box with argon atmosphere. The cell was introduced to the glove box through a antechamber. The used glove box is the LabMaster Pro Eco glovebox (MBRAUN).

The extracted materials were cleaned before taking them out of the glove box to measure the thermal conductivity. The cathode active material and the active anode material were washed using Dimethyl Carbonate solvent for two minutes for the cathode and 20 seconds (two 10 seconds steps) for the anode. The materials were dried inside the glove box for 24 hours before taking them out of the box.

3.2.2 Preparing of samples

Samples were cut off using a hammer and cutting tool with a diameter of 21 ± 0.1 mm. Then the thickness of each sample measured using a manual micrometre. For more accurate results, the thickness was measured at three different places to obtain an average thickness value. An Excel file has been created in the Lab-View folder for every new measured material. The Excel file contains thickness measurements, the order of sample stacking, the name of the material, and thermal conductivity for the rig steel.

3.3 Measurement settings

3.3.1 For dry measurements

In order to measure the thermal conductivity of anode and cathode samples, two current collectors foil samples with the same diameter were added between the electrode sample and the rig cylinder thermal contact between the apparatus and the sample. The applied pressure and time steps for dry measurements presented in table 3.2:

Tabell 3.2: Pressure and time steps for dry measurements.

Pressure	2.7 bar	4.6 bar	6.9 bar	9.2 bar	11.5 bar	11.6 bar	2.7 bar
Time	15 min	10 min	10 min	10 min	10 min	10 min	10 min

3.3.2 For wet measurements

For the wet measurement, the materials were soaked in electrolyte solvent before the measurement. The used solvent is Diethyl Carbonate (DEC). The samples were soaked for 30 minutes prior to the measurement. To avoid evaporation of the solvent from the sample during testing, a piece of tape was added around the sample before putting the isolation on. The applied pressure and time steps for wet measurements are presented in table 3.2:

Tabell 3.3: Pressure and time steps for wet measurements.

Pressure	2.7 bar	4.6 bar	6.9 bar	9.2 bar	11.5 bar	11.6 bar	2.7 bar
Time	10 min	5 min	5 min	5 min	5 min	5 min	5 min

3.4 Calculations

3.4.1 Thermal conductivity

A Matlab code written by Bern K. Holkenborg is used to calculate the thermal resistance and thermal conductivity of the samples from the measured temperatures and thickness values. The code is based on equations described in detail by Richter et al. [7]. The calculation starts by determining the heat flux over the sample using the equation 3.1:

$$q_{sample} = \frac{q_{upper}}{q_{lower}}, q_{upper} = k_{steel}\frac{T_1 - T_3}{d_{1-3}}, q_{lower} = k_{steel}\frac{T_6 - T_8}{d_{6-8}} \tag{3.1}$$

- q_{upper}: The heat flux between points 1 and 3 (see figure 3.1).
- T_1 and T_3: The measured temperatures at points 1 and 3 on the upper part of the cylinder.
- q_{lower}: The heat flux between points 6 and 8.
- T_6 and T_8: The measured temperatures at points 6 and 8 on the lower part of the cylinder.
- k_{steel}: The thermal conductivity for the rig stainless steel.

The thermal resistance of the sample is determined from the equation 3.2. Where $T_4 - T_5$ is the temperature drop over the sample and q_{sample} is the heat flux over the sample.

$$R_{sample} = \frac{T_4 - T_5}{q_{sample}} \tag{3.2}$$

The thermal resistance measured this way includes a thermal contact resistance between the sample and the measurement rig $R_{Rig-Sample}$, see figure 3.3. To be able to differentiate between the thermal resistance of the sample and the thermal contact resistance between rig and sample, several samples from the same materials with different thicknesses have to be measured. Different sample thicknesses are obtained by stacking several samples.

The total measured thermal resistance can be seen in the equation 3.3. Where $R_{Rig-Sample}$ is the thermal contact resistance between the sample and the measurement rig, R_{Sample} is the thermal resistance of the sample and R_{cc} the thermal resistance of the current collector. The thermal resistance of the current collector is negligible because its relatively high thermal conductivity [7].

$$R_{total} = 2R_{Rig-Sample} + R_{Sample} + R_{cc} \tag{3.3}$$

By plotting this sum of thermal contact resistance and the thermal resistance of the sample and taking a linear regression over this plot, the thermal conductivity of the sample can be obtained as the inverse slope number of this line [7].

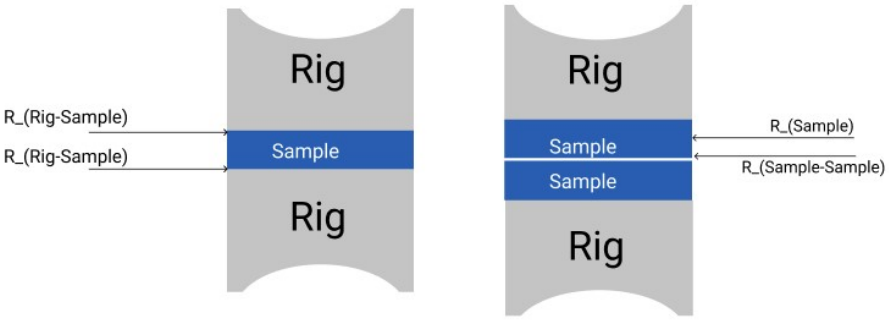

Figure 3.3: Total thermal resistance for measured samples.

In the case of anode and cathode, the measured thermal conductivity will be the electrode thermal conductivity, which means the conductivity for the current collector and the active material of the anode or cathode on both sides of the current collector.

The thermal conductivity of only the active material can be calculated by subtracting the current collector thickness from the total electrode sample thickness before plotting the total thermal resistance against the thickness. Then, taking a linear regression over this plot. The inverse slope number of this new line will be the thermal conductivity of just the anode or cathode active material.

3.4.2 Thermal model parameters

After measuring the thermal conductivity of all cell components, the simple thermal model described in section 2.4 is used to simulate the temperature distribution inside the battery. The entropy change ΔS of the electrode reaction, the specific ohmic resistance and the geometry parameters are presented in table 3.4.

Tabell 3.4: Input parameter for the thermal model.

Parameter	**LCO**	**NMC**
Number of single cells	24	24
Ambient temperature	290 K	290 K
Current density	13.1 A/m^2	35 A/m^2
Cathode thickness	90 μm	192μm
Anode thickness	104μm	204μm
Separator thickness	25 μm	25 μm
Current collector thickness	20 μm	20 μm
Entropy change	36 J/molK[27]	12 J/molK[27]
Ohmic resistance	0.033 Ohm m^2[28]	0.002 Ohm m^2[29]

3.5 Measuring thermal interface resistance

This section will describe in details a method to estimate the thermal interface resistance between the different cell layer (e.g. anode - separator, cathode - separator).

Thermal interface resistance

Usually, the cell component's thermal conductivity is measured for each layer separately. These values are then used to simulate a thermal model predicting the temperature distribution inside the battery [7]. But when the thermal conductivity for the whole battery is calculated, the thermal contact resistance between the cell layers is often neglected.

The thermal contact resistance between the separator and the electrode will be included in the total sample resistance by replacing the measured sample from one material ((e.g. anode separator cathode) with a sack of two separators and one electrode(e.g. anode - separator, cathode - separator). Further, comparing the measured total resistance from the stacked samples to the ones measured separately will determine the thermal contact resistance. Figure 3.4 shows how the samples are stacked for three tests.

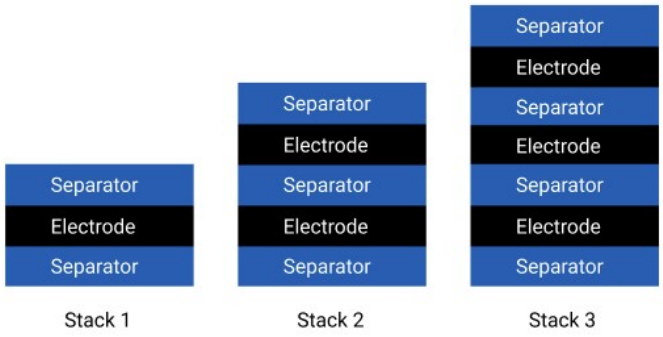

Figure 3.4: Sample stacking for the thermal contact resistance measurement.

In order to compare the values from this measurement to the one that done for the materials separately, the stacked samples measured dry and wet using the same time and pressure steps presented in section 3.3.1 for the dry and in section 3.3.2 for the wet measurements.

The new measured total sample resistance for the stacked samples will be as figure 3.5 shows for first stack, two times the thermal contact resistance between the separator and the rig $R_{Separator-Rig}$, two times the thermal resistance of the separator $R_{Separator}$, the thermal resistance of the electrode material $R_{Electrode}$ and two times the thermal contact resistance between the separator and the electrode $R_{Separator-Electrode}$ which is the wanted thermal contact resistance. Equation 3.4 shows the stacked sample total thermal resistance R_{total}.

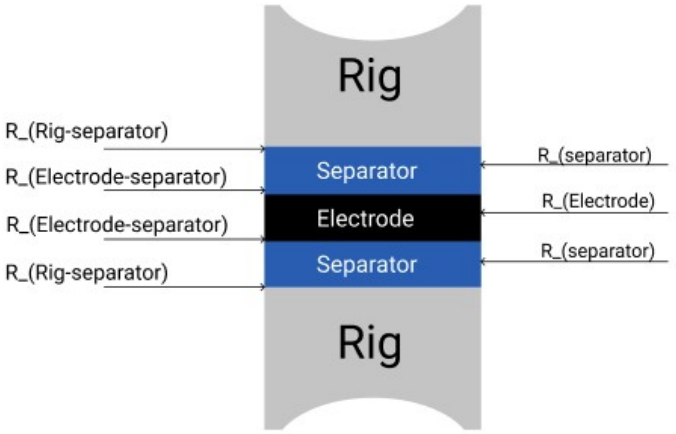

Figure 3.5: Total thermal resistance for measured samples.

$$R_{Total} = 2 * R_{Separator-Rig} + 2 * R_{Separator} + R_{Electrode} + 2 * R_{Electrode-separator} \tag{3.4}$$

From equation 3.4, replacing the $R_{Electrode}$ and $R_{Separator}$ with the thermal resistance from the measurement that done for each layer separately gives equation 3.5 with just one unknown led $R_{Electrode-separator}$ which will be the wanted thermal contact resistance between the separator and the electrode.

$$R_{Electrode-separator} = (R_{Total} - 2 * R_{Separator-Rig} - 2 * R_{Separator} - R_{Electrode})/2 \tag{3.5}$$

Impact on thermal conductivity

In order to study the impact of thermal contact resistance on the thermal conductivity and the thermal behaviour of the cell, equation 2.8 used to calculate the through-plane thermal conductivity for a cell with two separators and one electrode (anode or cathode). By comparing the calculated values to the values from stacking measurement, the difference between these two conductivity values will be the impact from the contact thermal resistance.

4 Results and Discussion

The following chapter presents and discusses the results for thermal conductivity measurements and analyses on both Custom and Melasta cells. Further, the simulated 1 D temperature distributions of both cell are presented. In addition, the results from comparing the fresh and beginning of life (BOL) material is reported. The results chapter ends with a section presenting the results from thermal interface resistance measurements.

4.1 Extracting electrodes from battery cell

A new Custom cell battery was opened to extract electrodes for thermal conductivity measurements and obtain more detailed information of the cell construction for modelling (e.g. number of layers, thickness). The battery was opened by following the procedure described in section 3.2.1. Figure 4.1 shows the opening stages inside the glovebox. Figure 4.1a shows the introduced battery after taping the tabs to avoid external short-circuiting during the opening process. The opening started by cutting the case cover at the edge of the cell, see figure 4.1b and 4.1c. This was done carefully to avoid cutting thru the cell layers, causing an electric current short-circuiting.

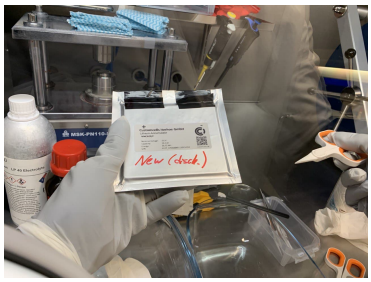

(a) The cell inside the glove box

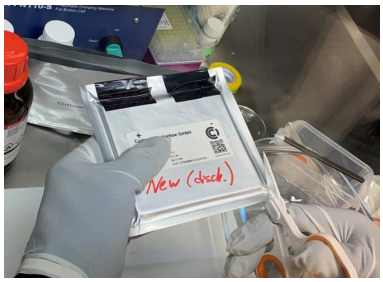

(b) Cutting the Sealed edge

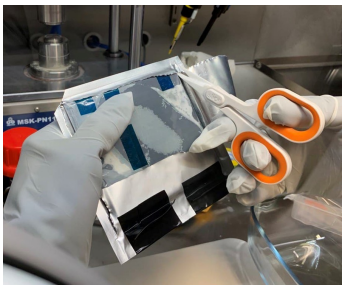

(c) Opening the case cover

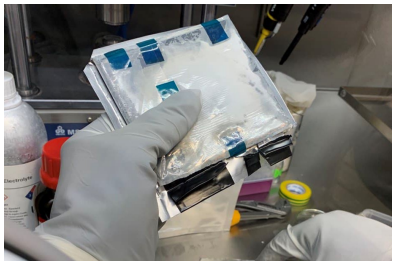

(d) The cell without the case

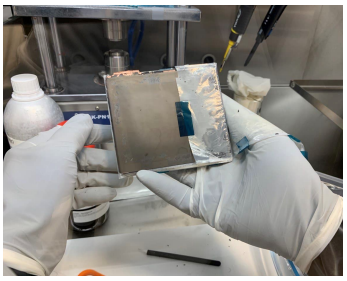

(e) The first anode layer

(f) Separating the cell layers

Figure 4.1: Opening the pouch NMC Cell inside the glove box

Figure 4.1d shows the cell after removing the case cover. The separator was folded around the entire battery cell and secured with tape. The last and first layer was coated with anode electrode material on both sides. On one side of the cell, the separator was taped to the first anode layer as shown in figure 4.1e. The separator was Z-folded around the electrodes. Finally, figure 4.1e shows the process of separating cell electrode layers from each other.

After removing a few anode layers, changes in the active material structure have been noticed. Figure 4.2a shows how the active material became brittle and fragile near the tabs. Some layers were affected more than others. Figure 4.2b shows how the active material for some layers stuck to the separator after removing the anode.

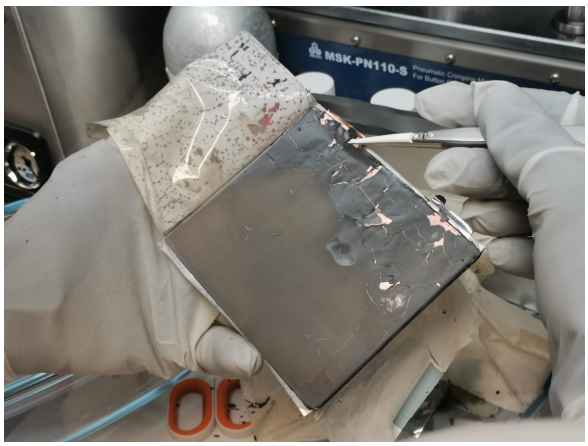

(a) The cell inside the glove box

(b) Cutting the Sealed edge

Figure 4.2: Custom cell anode layers inside the battery.

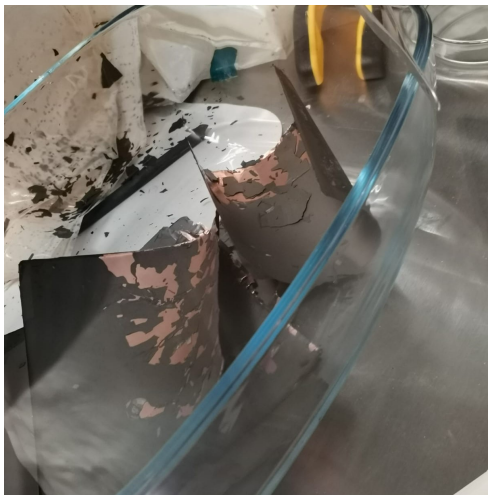

(a) Anode layer

(b) Cathode layer

Figure 4.3: Custom cell anode and cathode layers.

Figure 4.3b shows a cathode layer compared to an anode layer in figure 4.3a. The cathode layers seems to be not affected compared to the anodes. Before taking the cell materials outside the glove box for the thermal conductivity measurement, the materials were cleaned inside the glovebox by following the procedure described in section 3.2.1.

4.2 Thermal conductivity

The thermal conductivity measurements of the battery materials were done using the measurement setup described in section 3.1. Samples from separator, anode and cathode were peppered following procedure described in section 3.2.2. Time and applied pressure steps for dry measurements are presented in section 3.3.1 for dry measurements and in section 3.3.2 for wet measurements. The data collected from the measurement rig and send into the Matlab code described in section 3.4 to calculate the thermal conductivity.

4.2.1 Separator

Starting with calculating the thermal resistance for the separator using the method described in section 3.4.1 figure 4.4 shows the thermal resistance as a function of the sample thickness when the applied pressure is increased from 2.7 bar to 11.6 bar. The thermal resistance plotted in this figure is the sum of separator thermal resistance and thermal contact resistance between the measurement rig and the separator samples.

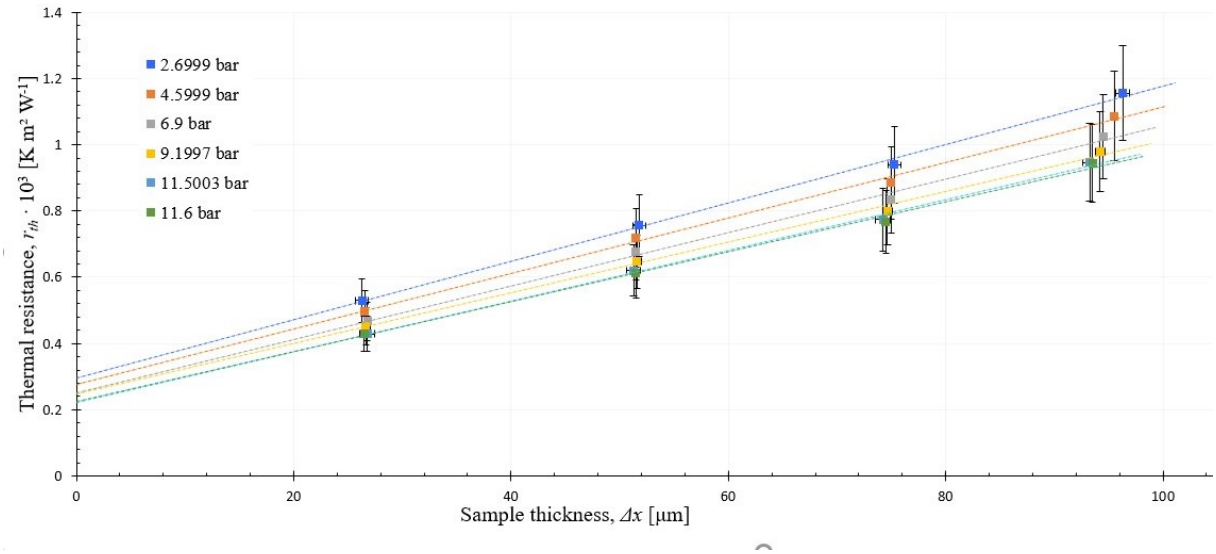

Figure 4.4: Thermal resistance for dry separator as a function of applied pressure.

The plot shows how the thermal resistance from the first stack (sample with thickness of 25 μm) decreases from 5.6 ± 0.7 E-04 Km^2w^{-1} at 2.7 bar to 4.6 ± 0.5 E-04 Km^2w^{-1} at 11.6 bar compaction pressure. On the fourth test (samples with thickness 95 μm), the effect of the applied pressure can be seen clearly; the thickness decreases from 96.3 μm at 2.7 bar to 93.5 μm at 11.6 bar.

Furthermore, the thermal conductivity of the separator was calculated. The thermal conductivity increased from 0.113 $Wk^{-1}m^{-1}$ at 2.7 bar applied pressure to 0.132 $Wk^{-1}m^{-1}$ at 11.6 bar. A figure shows the effect of applied pressure on the separator conductivity is added to section 4.3.1.

4.2.2 Anode layers

Table 4.1 presented the measured effective thermal conductivities for dry anode layers from both Custom and Melasta cells when the compaction pressure was increased in the range of 2.7 to 11.6 bar. The thermal conductivity values were measured for the total electrode (the current collector and the coated active materials on both side of the current collector). The thermal conductivities for the anode active material are presented as well. The measurements for both cells have been conducted by using the same applied pressure and time steps.

Tabell 4.1: Measured thermal conductivity for dry anode layers. $Wk^{-1}m^{-1}$.

P[bar]	$K^{CC}_{A-electrode(fresh)}$	$K^{CC}_{A-a.m(fresh)}$	$K^{ML}_{A-electrode(BOL)}$	$K^{ML}_{A-a.m(BOL)}$
2.7	0.427 ± 0.008	0.398 ± 0.008	0.6 ± 0.2	0.56 ± 0.18
4.6	0.478 ± 0.006	0.445 ± 0.006	0.8 ± 0.3	0.7 ± 0.2
6.9	0.526 ± 0.017	0.489 ± 0.016	0.9 ± 0.3	0.8 ± 0.3
9.2	0.56 ± 0.02	0.52 ± 0.02	0.9 ± 0.4	0.8 ± 0.3
11.5	0.595 ± 0.019	0.553 ± 0.019	1.0 ± 0.4	0.9 ± 0.3
11.6	0.597 ± 0.018	0.554 ± 0.017	1.1 ± 0.4	0.9 ± 0.3

ML = Melasta Cell

CC = Custom Cell

A-a.m = Anode active material

BOL =Beginning of life

The Custom cell anode measurement showed low standard deviation of 1 - 3 % of the measured thermal conductivities values, while the Melasta anode measurement shows a larger error of 32-38 %. The large standard deviation in the conductivity values for the Melasta cell is due to the total thermal resistance values that were not entirely linear. A figure showing the thermal resistance of the Melasta anode as a function of the sample thickness is added to the appendix A in figure A.1. There are other factors that can affect the measured thermal conductivity values and the thermal resistance; some will be described and discussed later on in section 4.4.

The Custom cell anode thermal conductivities increases by 40% from 0.427 $Wk^{-1}m^{-1}$ to 0.597 $Wk^{-1}m^{-1}$ when the compaction pressure increased from 2.7 bar to 11.6 bar. A more rough structure could explain the dependence of the thermal conductivity on pressure. The Melasta cell anode measurement showed higher dependency on the applied compaction pressure where the measured thermal conductivity increases nearly 83% from 0.60 $Wk^{-1}m^{-1}$ at low pressure to 1.05 $Wk^{-1}m^{-1}$ at the highest applied pressure.

Calculation of the thermal conductivity of the active material is done as described in section 3.4.1. The results from the Custom cell anode active material measurement show that the thermal conductivities of the active material is lower than the electrode conductivities by around 0.03 $Wk^{-1}m^{-1}$. In the case of Melasta anode, the calculated values are lower by around 0.1 $Wk^{-1}m^{-1}$.

4.2.3 Cathode layers

The cathode active material for the Custom cell called NMC622(Nickel Manganese Cobalt). While the Maleasta cell cathode is based on LiCoO2(Lithium Cobalt Oxyde). Table 4.2 presents the measured thermal conductivities for the two dry cathode electrodes. The results showed an increase in the thermal conductivity values for the NMC cathode (electrode) by around 9 %for a range of applied compaction pressure of 2.7 - 11.6 bar, while the LCO cathode (electrode) conductivities increased by 27 %.

Tabell 4.2: Measured thermal conductivity for dry cathode layers. $Wk^{-1}m^{-1}$.

P[bar]	$K^{CC}_{C-electrode(fresh)}$	$K^{CC}_{C-a.m(fresh)}$	$K^{ML}_{C-electrode(BOL)}$	$K^{ML}_{C-a.m(BOL)}$
2.7	0.35 ± 0.05	0.32 ± 0.04	0.51 ± 0.06	0.41 ± 0.05
4.6	0.36 ± 0.04	0.32 ± 0.03	0.54 ± 0.07	0.44 ± 0.06
6.9	0.37 ± 0.03	0.33 ± 0.03	0.58 ± 0.11	0.47 ± 0.09
9.2	0.37 ± 0.03	0.34 ± 0.03	0.62 ± 0.13	0.50 ± 0.11
11.5	0.37 ± 0.03	0.34 ± 0.03	0.64 ± 0.12	0.52 ± 0.10
11.6	0.38 ± 0.03	0.34 ± 0.03	0.65 ± 0.14	0.52 ± 0.11

CC = Custom Cell

ML = Melasta Cell

C-a.m = Cathode active material

BOL =Beginning of life

Thermal conductivities of cathode active materials are measured for both Custom and Melasta cells. see table 4.2. The measured thermal conductivity for cathode active material reported in the range of 0.32 - 0.554 $Wk^{-1}m^{-1}$ for the MNC cathode and 0.41 - 0.52 $Wk^{-1}m^{-1}$ for the LCO cathode.

When comparing the cathode layers thermal conductivity measurements to the anode layers, results showed a higher dependency on the compaction pressure then for the anode conductivities. The Custom Cell cathode thermal conductivity increased by 8 %, while the anode conductivity increased by 40 %. The thermal conductivity of the Melasta cell cathode layer increased by 21 %, while the anode conductivity increased by 83%.

The total thermal resistance from the dry measurements for both cell added to the appendix A in table A.1.

4.3 Electrolyte impact

In order to understand the impact of the electrolyte on the thermal conductivity of the LIB materials, all materials were measured soaked in the electrolyte solvent as well. Overview over which materials measured at which condition added in section 3.2.

4.3.1 Wet measurements

Thermal conductivity for solvent soaked samples from separator, anodes and cathodes were measured following the procedure described in section 3.3.2. Time and applied pressure steps for wet measurements are presented in table 3.3.

Separator

The thermal conductivity wet measurements start with measuring the separator conductivity. The first measurement for electrolyte solvent soaked separator done using the same time steeps used for dry measurement. Figure 4.5 shows the first separator thermal conductivity as a function of applied pressure (red). The results were not as expected, where the thermal conductivity started decreasing after the third pressure step and continued to drop until it reached 0.216 $Wk^{-1}m^{-1}$ at 11.6 bar, which is close to the dry separator conductivity (plotted in figure 4.5 in blue colour). An evaporation of the electrolyte solvent from the samples during the measurement explains the decrease in thermal conductivity. The large measurement errors for the pressure steps in the middle are due to the difference in the measured thicknesses of the samples between fully wet at the start and dry at the last steps.

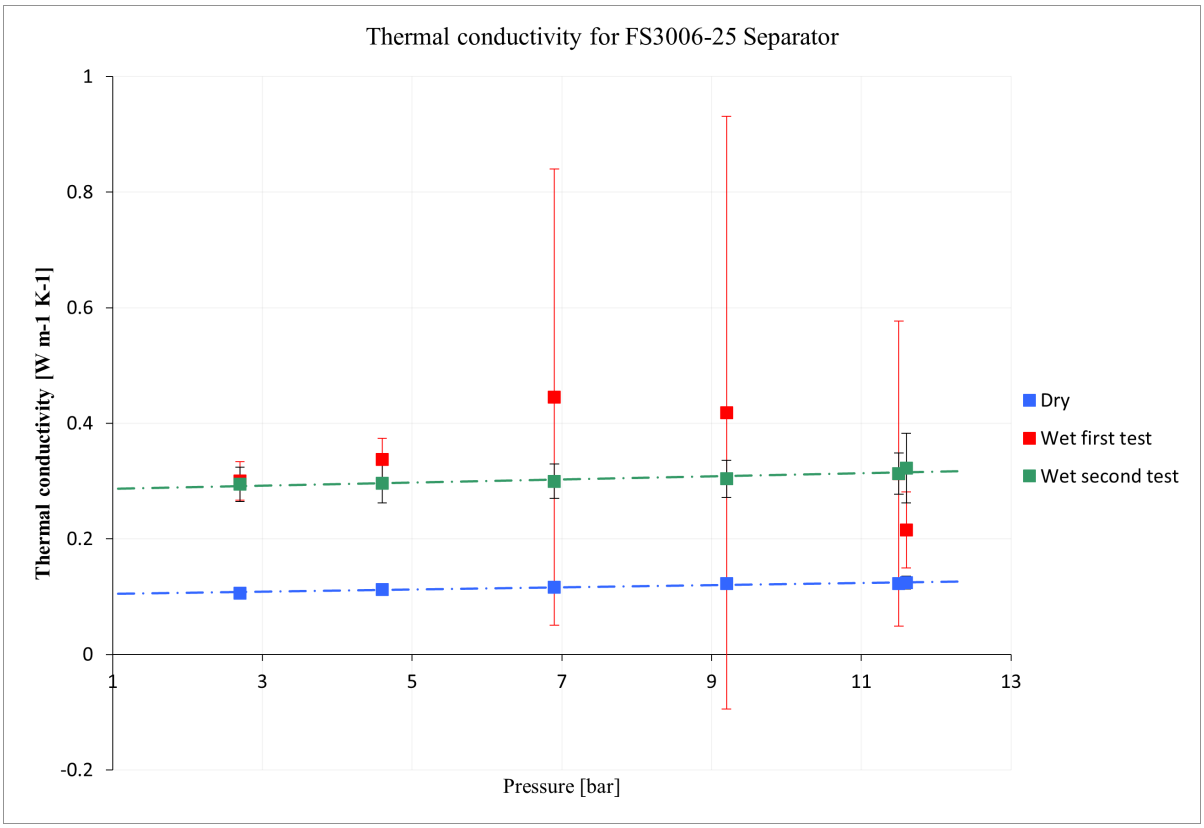

Figure 4.5: Thermal conductivity for FS3006-25 separator.

The decrease of conductivity started after the third pressure step, which means the sample started drying after around 30 minutes from the start of the measurement. For the second measurements, time steps were reduced to half of the dry measurement time. Table 3.3 shows the used time steps at all applied pressure steps.

The second measurement for the separator shows more accuracy and stable results for the thermal conductivity, as seen in figure 4.5 (in green). Table 4.3 show the measured thermal conductivity values for dry and electrolyte solvent wet separator at all applied pressure steps. Thermal conductivity for the wetted separator from second measurement starts at 0.29 $Wk^{-1}m^{-1}$ for 2.7 bar and increase to 0.32 $Wk^{-1}m^{-1}$ for 11.6 bar.

Tabell 4.3: Thermal conductivity for the separator dry and wet measurements $Wk^{-1}m^{-1}$.

P[bar]	$K^{dry}_{Separator}$	$K^{wet.1}_{Separator}$	$K^{wet.2}_{Separator}$
2.7	0.106 ± 0.008	0.30 ± 0.03	0.29 ± 0.02
4.6	0.112 ± 0.008	0.34 ± 0.03	0.30 ± 0.03
6.9	0.116 ± 0.012	0.5 ± 0.4	0.30 ± 0.02
9.2	0.123 ± 0.011	0.4 ± 0.5	0.30 ± 0.03
11.5	0.123 ± 0.009	0.3 ± 0.2	0.31 ± 0.03
11.6	0.124 ± 0.012	0.22 ± 0.06	0.32 ± 0.06

Separator thermal conductivity increased by factor of 3, from 0.11 $Wk^{-1}m^{-1}$ at 2.7 bar to 0.29 $Wk^{-1}m^{-1}$ by adding the electrolyte solvent to the samples. See figure 4.5. Richter et al.[7] reported the thermal conductivity for the same separator in Table 2 for both dry and wet measurements. Reported values increased with around the same factors when soaking the sample in electrolyte solvent. The reported values could not be directly compared to those measured in this study because of the different pressure steps and electrolyte solvent used in the experiment.

Adding the electrolyte solvent to the samples decreased the thermal resistance for the wetted separator to be around 33 % of the dry separator thermal resistance. The measured thermal resistance for the dry and wetted separator samples added to appendix A in table A.2.

Anode and Cathode layers

All the electrodes that used for this part of the study are at the beginning of life. Table 4.4 present the thermal conductivity for wetted anode and cathode from both Custom and Melasta cells. The thermal conductivity values presented in this section are for the whole electrode (the current collector and the active material coated on both side). The samples soaked entirely in the Diethyl carbonate electrolyte solvent for about 30 minutes before the test. The used compaction pressure steps are the same as the dry measurements.

Tabell 4.4: Thermal conductivity for anode and cathode wet measurement.

P[bar]	$K^{CC}_{Anode(BOL)}$	$K^{CC}_{Cathode(BOL)}$	$K^{ML}_{Anode(BOL)}$	$K^{ML}_{Cathode(BOL)}$
2.7	1.6 ± 0.9	0.87 ± 0.03	1.3 ± 1.2	1.3 ± 0.2
4.6	1.7 ± 0.9	0.88 ± 0.03	1.6 ± 1.6	1.3 ± 0.3
6.9	1.8 ± 0.9	0.87 ± 0.02	2 ± 2	1.4 ± 0.3
9.2	1.9 ± 0.9	0.87 ± 0.02	2 ± 3	1.6 ± 0.3
11.5	1.9 ± 0.8	0.88 ± 0.03	3 ± 3	1.6 ± 0.3
11.6	2.0 ± 0.9	0.89 ± 0.04	3 ± 3	1.6 ± 0.3

CC = Custom Cell

ML = Melasta Cell

BOL =Beginning of life

Starting with the Custom cell layers, the wetted cathode measurement showed low dependency on the compaction pressure, where the thermal conductivity increased with 2 % from 0.87 to 0.89 $Wk^{-1}m^{-1}$. While the wetted anode thermal conductivity reported in the range of 1.6 - 2.0 $Wk^{-1}m^{-1}$ giving an increase of around 2 %. In the case of Melasta cell, the dependency on the compaction pressure was higher, where the increase reached 100 % for the anode samples thermal conductivity and around 24 % for the cathode.

When comparing the values from the dry measurements presented in section 4.2.2 to the results presented in table 4.4 the electrolyte effect on the thermal conductivity can be determined. Soaked samples showed a significantly higher thermal conductivity. Comparing these values show at the thermal conductivity of the Custom cell graphite anode has the highest dependency on electrolyte solvent soaking, where the effect was a factor of about 4. In comparison, the effect on the Melasta cell anode was a factor of about 2. The cathode thermal conductivity increased by about 3 for the Melasta cell and about 2 for the Custom cell. A difference in the structure (particle size or porosity) of these two anodes could explain the electrolyte dependency differences.

Soaked anode samples results showed a higher standard deviation than for the cathode samples. The chemistry difference between the anode and the cathode active material could be an explanation for that. Another factor could be that the used anode is extracted from a battery cell at BOL phase, more discussion about this presented in section 4.4.

Richter et al.[7] reported the thermal conductivity for similar material at 2.3 bar compaction pressure; the paper reported in table 2 thermal conductivity of 1.51 $\pm$ 0.12 $Wk^{-1}m^{-1}$ for a wetted LCO cathode from manufacture called Hohsen. The Melasta LCO cathode showed lower conductivity at 1.3 $\pm$ 0.2 $Wk^{-1}m^{-1}$. In table 5 the paper reported 1.09 $\pm$ 0.10 $Wk^{-1}m^{-1}$ for a wetted NMC cathode from XALT manufacture. The NMC cathode from the Custom cell showed 1.6 $\pm$ 0.9 $Wk^{-1}m^{-1}$ at 2.7 bar. The difference in applied pressure could be an explanation of the difference on the thermal conductivities between the literature and this study.

The thermal conductivities for the cathode from both cells are plotted as a function of the applied pressure in figure 4.6. The standard deviations are included in the plot. The figure shows that the LCO cathode has higher thermal conductivity than the NMC cathode from the Custom cell for both dry and soaked samples measurements.

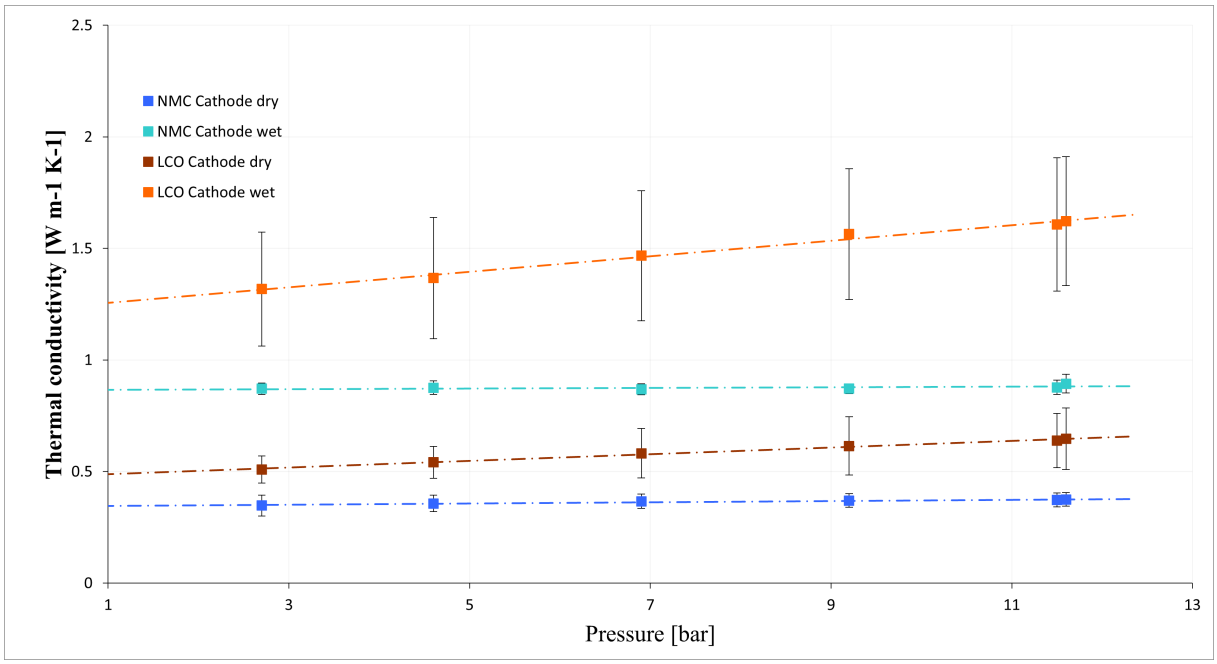

Figure 4.6: Thermal conductivity for NMC and LCO cathodes (dry and wet) as a function of applied pressure.

Using the anode thermal conductivity values presented in table 4.1 for dry measurements and in table 4.4 for wet measurements a figure showing the thermal conductivity for the anode measurement from both cells added to the appendix A in figure A.2.

4.3.2 Thermal models

The simple 1D thermal model described in section 2.4.2 is used to simulate both cells internal temperature distribution. The model input parameters presented in section 3.4.2. In the model, the thermal conductivity values from dry measurements used at 2.7 bar for all cell layers. Furthermore, In order to understand the electrolyte impact on the thermal conductivity and the temperature distribution inside the cell, another model simulated using the thermal conductivity values from the wetted samples measurements at the same pressure (i.e., 2.7 bar). The simulated models plotted in figure 4.7a for the Custom cell and figure 4.7b for the Melasta cell.

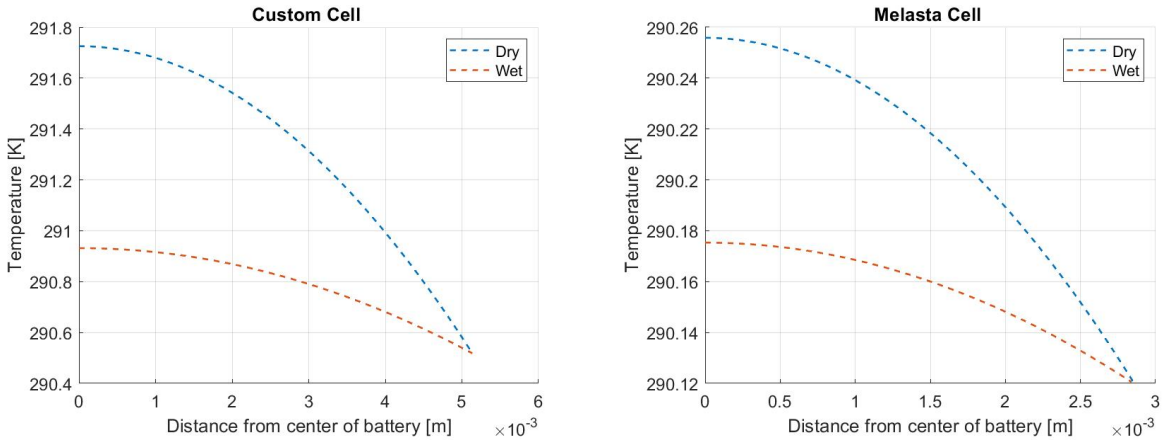

(a) Custom cell charging.

(b) Melasta cell charging.

Figure 4.7: 1D temperature profile for Custom and Melasta cell during charging.

The temperature at the centre of the dry Custom cell battery during charging calculated to be 291.7 K for the dry battery and 290.9 K for the wet battery. The surface temperature calculated to be 290.5 k. Results showed a temperature difference of about 1.2 K from the centre to the surface of the dry and about 0.4 for the wet battery. Adding the electrolyte solvent to the battery layers decreased the centre temperature by about 0.8 K.

In the case of the Melasta cell, the temperature difference between the centre and the surface calculated to be about 0,8 K for the dry battery and 0.06 K for the wetted. The impact of electrolyte solvent on the Melasta battery centre temperature determined to be 0.08 K.

A thermal model simulate both cells internal temperature distribution during discharging added to appendix A in figure A.3.

4.4 Aging impact

In the following, the impact of Custom cell battery ageing on the cell electrodes thermal conductivity are investigated.

The Custom cell electrode layers used for this measurement were at two different life phase. Fresh anode and cathode layers received directly from the manufacturer, which means that the material has never been in a battery cell. The other electrode materials are from the same batch, but they were assembled into a cell and underwent some formation and storage, that means at the cell has not cycled or used. Still, some charging and discharging tests have been done by the manufacturer on the battery cell to do a cell quality check.

Due to the available amount of fresh materials in the lab, this study is done only on the dry materials (i.e. Fresh dry and BOL dry). For more specific results, thermal conductivity values from just anode active material and cathode active material are used in this study.

Material extraction, cleaning and samples preparing for the measurements are described in detail in section 4.1. Fresh anode active material and cathode active material thermal conductivity are presented in table 4.1 for the anode and table 4.2 for the cathode. Thermal conductivity values for the BOL electrodes are attached to the appendix A on table A.3. The thermal conductivity from both cathodes measurements are plotted in figure 4.8.

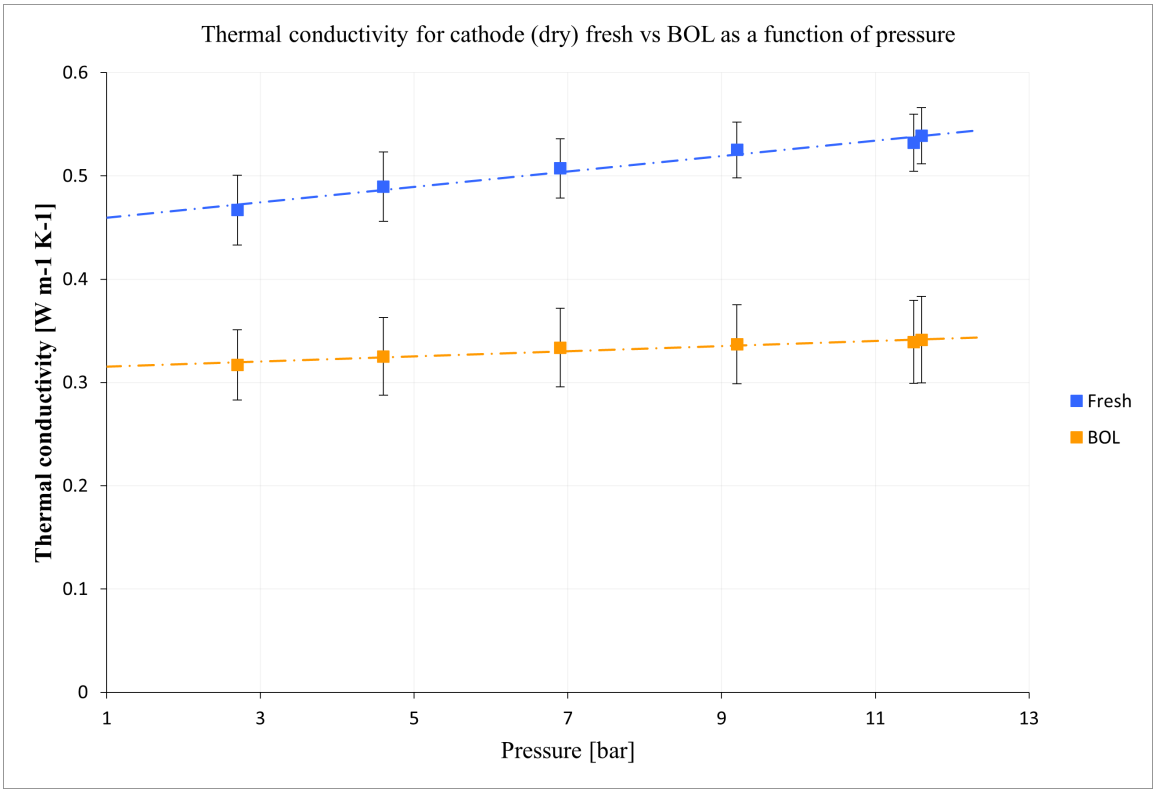

Figure 4.8: Thermal conductivity for cathode dry fresh vs dry BOL as a function of applied pressure.

The results showed higher thermal conductivity for the fresh cathode active material. At low pressure the extracted cathode showed decrease in the thermal conductivity by 32 % Form 0.47 $Wk^{-1}m^{-1}$ for the fresh to 0.32 $Wk^{-1}m^{-1}$ for the BOL cathode. At high pressure thermal conductivity decreased by 37 % from 0.54 $Wk^{-1}m^{-1}$ to 0.34 $Wk^{-1}m^{-1}$.

The thermal conductivity of fresh and BOL anodes plotted as a function of applied pressure in figure 4.9.

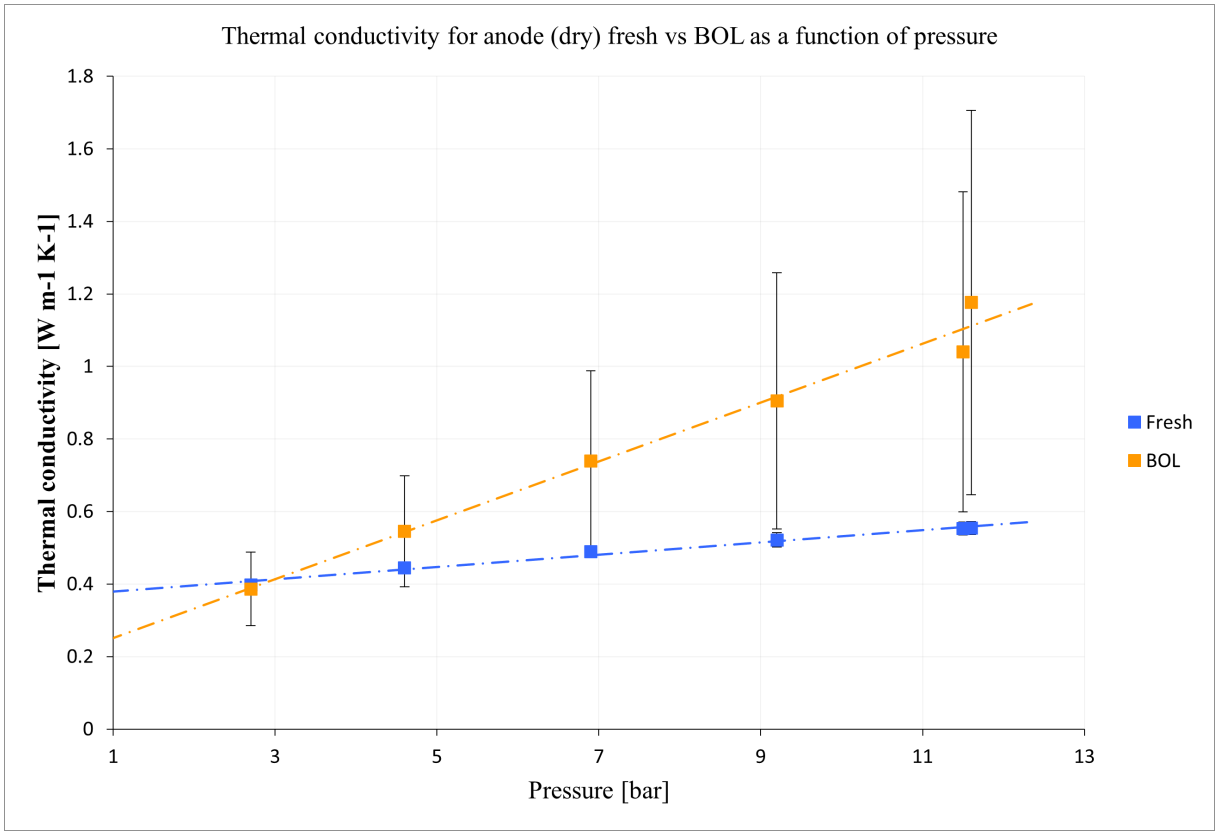

Figure 4.9: Thermal conductivity for Anode dry fresh vs dry BOL as a function of applied pressure.

Unlike the cathode measurement, the anode measurements showed lower thermal conductivity for the extracted samples at 2.7 bar pressure, but the conductivities increased significantly for higher pressure steps. The compaction pressure increased the thermal conductivity with 41 % for the fresh anode and 208 % for the BOL anode. The standard deviations of the measured thermal conductivity values for the extracted material were very high.

The expansion in the structure of the extracted cathode's active materials could explain the decrease of the BOL cathode thermal conductivities. Sauerteig et al. at [30] explained how the charging and discharging processes leads to expansion and contraction of the active materials of the LIB electrodes. Since the BOL cell has been cycled at least once during the testing, a sustained expansion of the cathode active material could affect the cathode capability to conduct

heat. It also has been noticed a change in the thickness of the samples when they are measured manually before the conductivity measurement; the BOL cathode sample thickness was about 197 μm where the fresh ones were about 192 μm.

The electrolyte effect on the cathode active material (described in section 4.3) could be another factor that caused this difference in the thermal conductivity values. Since the cathode layers were soaked in the electrolyte solvent inside the battery cell then were dried when the cell was opened, then wetted and dried for a second time when the materials cleaned before measuring the thermal conductivity, the possibility of leftover solvent in some of the tiny pores in the active material structure could affect the conductivity abilities of the active materials.

The results from the extracted anode thermal conductivity measurements showed a large error and large difference in pressure dependency compared to the fresh material. The brittle structure of the extracted materials may have led to these large errors in the conductivity measurements, where the extracted materials thicknesses effected by the compaction pressure. A description of the extracted materials structure when the cell was opened added to section 4.1.

Another critical factor that may affect the results of the anode measurements is the status of the measured samples. The extracted anode layer active material was fragile; The samples cutting removed a part of the active material at the edge of the sample. Figure 4.10 show the samples from extracted anodes on the right-hand side compared to the samples from the fresh material on the left-hand side. Compared to the active material, especially at high pressure, the high conductivity of the current collector might have resulted in very uneven heat flow over the sample.

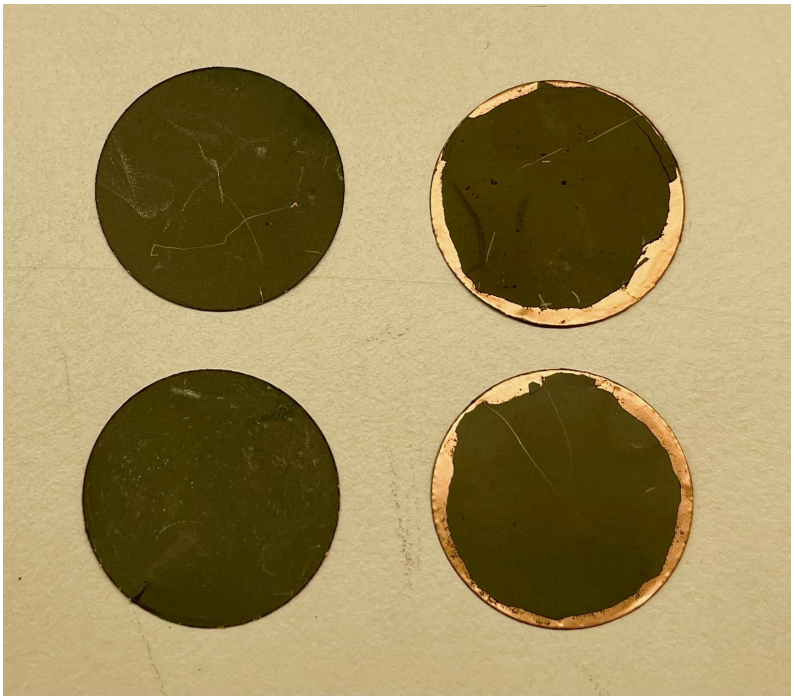

Figure 4.10: Anode samples fresh vs extracted.

4.5 Thermal interface resistance

In the following, the thermal interface resistance between the cell layer is measured. Its effect on the thermal conductivity and the thermal behaviour of the cell is determined. A complete description of the used method and equations was presented in section 3.5 of the method chapter.

4.5.1 Stacked samples measurements

The first stacked measurement is done on the Melasta cell (anode - separator) samples. The samples stacked in order (anode - separator - anode), then one separator and one anode added on the second stack and two to the third stack. Then a thin layer from the current collector added where the stacked samples are in contact with the measurement rig. Stacking the samples on one line between the rig cylinders was challenging, especially at the last test (stuck 3) where the number of the stacked samples were 9 (4 anodes, 3 separators and 2 current collectors). After this measurement, the samples stacked in the order showed in figure 3.4, starting and ending with separator samples, that helped reduce the two current collector layers.

The thermal conductivity values for the staking of (anode - separator) and (cathode - separator) measurements presented in table 4.5 at 2.7 bar pressure. The table present the measured thermal conductivities for the stacked samples at all pressure steps are added to appendix B in table B.1.

Tabell 4.5: Thermal conductivity and thermal resistance for Melasta layers stacked at 2.7 bar.

Layer	$K^{ML}\ Wk^{-1}m^{-1}$	$R^{ML}_{total}\ Km^2w^{-1}$
ML^{dry}_{C-S}	0.32 ± 0.03	(1.08 ± 0.12)E-03
ML^{wet}_{C-S}	0.82 ± 0.05	(0.4 ± 0.4)E-03
ML^{dry}_{A-S}	0.35 ± 0.13	(1.4 ± 1.8)E-03
ML^{wet}_{A-S}	1.1 ± 0.8	(0.4 ± 0.3)E-03
CC^{dry}_{C-S}	0.387 ± 0.016	(1.5 ± 0.2)E-03
CC^{dry}_{A-S}	0.4 ± 0.1	(0.61 ± 0.07)E-03

S_C = Separator - Cathode

S_A = Separator - Anode

The materials used in this measurement were extracted from the battery cell at BOL. The anode-separator from the Custom cell showed higher thermal conductivity than the fresh anode measured individually, which means this stacking measurement could not be used in determining the thermal interface resistance. The effect in the BOL anode structure could be an explanation for the higher thermal conductivity (see section 4.4).

The total thermal resistance values for the stacked samples are reported in table 4.5 at 2.7 bar. The results were as expected showed higher total thermal resistance for the stacked samples compared to the sum of the resistance of the layers measured separately.

The total thermal resistance for the Melasta cell dry (cathode - separator) measured to be 1.08 E-3 Km^2w^{-1} at 2.7 bar. The sum of the thermal resistances of the same materials measured individually is calculated to be 0.7 E-3 Km^2w^{-1}. The difference between these two values is the sum of the thermal contact resistance between the stacked samples and the rig and the thermal contact resistance between the cathode and the separator. Using equation 3.5 the values for the thermal contact resistance between the cell layers were calculated. Table 4.6 presents the calculated thermal interface resistance between the Melasta cell layers dry and wetted.

Tabell 4.6: Thermal interface resistance for the Melasta cell cathode-Sep and anode-Sep.

P[bar]	R^{dry}_{C-S} E-05	R^{wet}_{C-S}E-05	R^{dry}_{A-S}E-05	R^{wet}_{A-S}E-05
2.7	4.3 ± 1.8	1.69 ± 0.09	6.5 ± 1.4	0.2 ± 1.6
4.6	3.9 ± 0.9	1.72 ± 0.12	5.6 ± 1.2	0.6 ± 1.5
6.9	3.4 ± 0.6	1.5 ± 0.2	4.9 ± 0.9	0.5 ± 1.7
9.7	3.3 ± 0.6	1.5 ± 0.2	4.3 ± 0.7	0.4 ± 1.6
11.5	2.1 ± 0.6	1.7 ± 0.2	3.8 ± 0.3	0.7 ± 1.5
11.6	2.16 ± 0.07	2.1 ± 0.4	3.8 ± 0.3	1.1 ± 1.0

S_C = Separator - Cathode

S_A = Separator - Anode

Figure 4.11 shows how the applied pressure effect the thermal interface resistance between the dry LCO cathode and the separator.

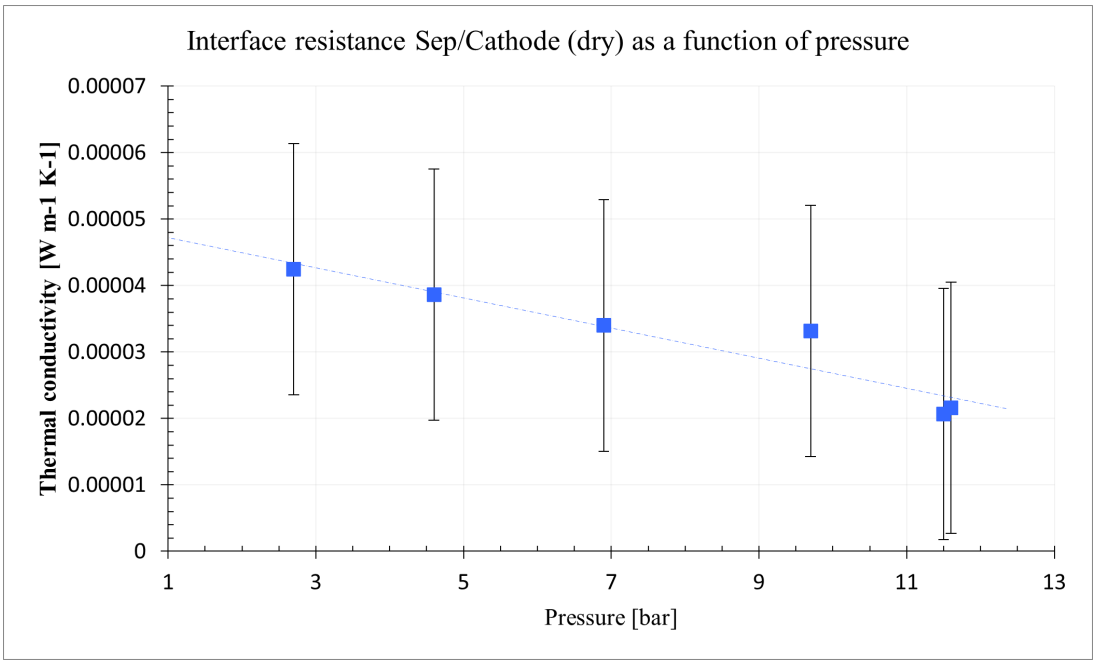

Figure 4.11: Contact resistance between separator/Cathode (dry) as a function of pressure

4.5.2 Impact on thermal conductivity

In order to compare the measured thermal conductivity from the stacked samples, the effective thermal conductivity for a cell with the same combination of layers is calculated using equation 2.8, the thermal conductivities for each layer separately are presented in sections 4.2 and 4.3. The effective thermal conductivity for stacked samples is calculated for both dry and wet cell layers. Table B.2 is added to appendix B presents these values at all pressure steps. Measured and calculated effective thermal conductivity of dry and wet stacked Separator-Cathode samples is plotted as a function of the applied pressure in figure 4.12.

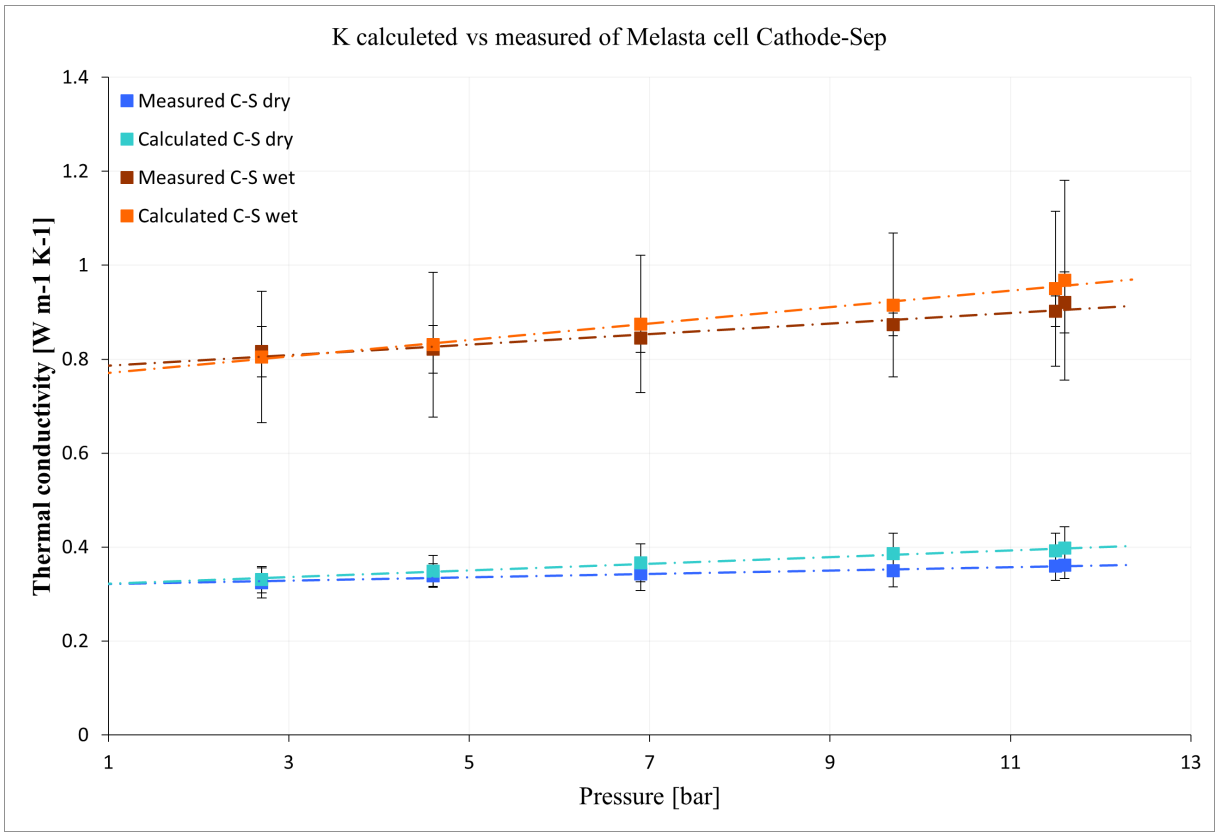

Figure 4.12: Thermal conductivity of the LCO Cathode-Separator as a function of applied pressure.

The relative high errors in the calculated thermal conductivity for wetted Separator-cathode are due to the wetted LCO cathode measurement errors. (see table 4.3.1). The comparing of the thermal conductivities showed unexpected results. The difference between the measured and the calculated values increased with the compaction pressure. The differences expected to be high at low-pressure steps where the thermal contact resistance is highest. The figure shows the thermal contact resistance as a function of the applied pressure is added to appendix B in figure B.3.

Figure B.1 shows the anode-separator stacked thermal conductivity dry and wetted measurements. The effective thermal conductivity is plotted at the same graph showing the impact of the thermal interface resistance on the thermal conductivity for the anode-Separator stacked samples. B

4.5.3 Thermal models

Another way to understand the effect of the thermal interface resistance between the cell layers is by simulating the temperature profiles inside the battery. In order to do that, the same thermal model that used on the Melasta cell layers separately is used on the measured thermal conductivities from the stacked samples; this will include the thermal interface resistance in the model. All other input parameters were kept constant to shows only the effect of the thermal interface resistance. The models are plotted in figure 4.13.

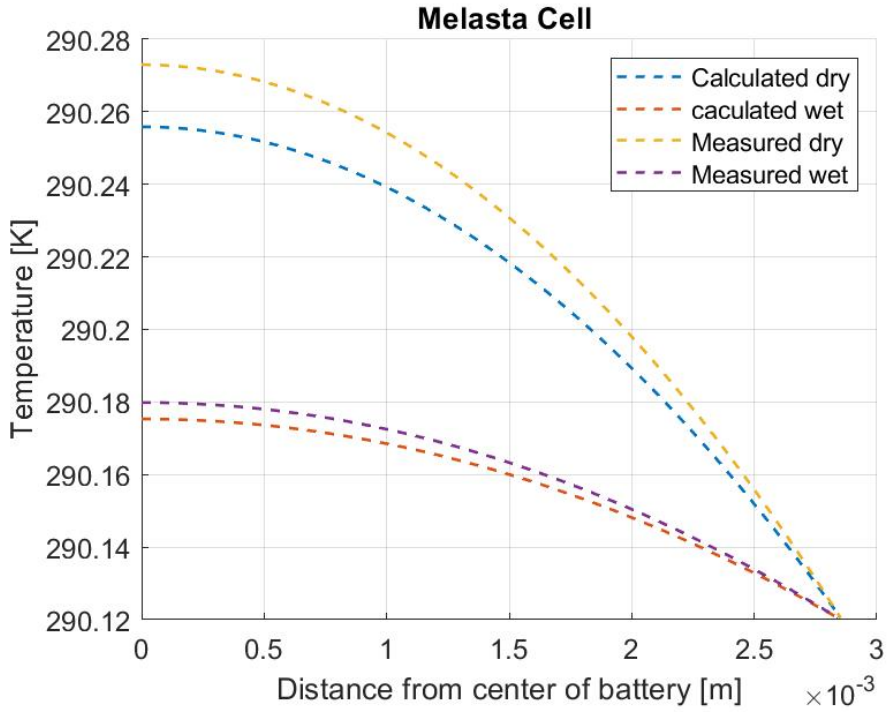

Figure 4.13: Temperature distribution in the Melasta cell during charge including the thermal interface resistance effect on the effective thermal conductivity.

The temperature profile showed expected results. Due to the thermal interface resistance, the centre temperature during charging increased (more thermal resistance means a slower heat transport). The increase was higher in the case of dry cell layers, where the thermal interface resistance was higher. The temperature difference at the centre of the battery is about 0.02 K. and 0.01 K using the measured conductivity from the wetted stuck.

5 Conclusion

5.1 Conclusion

This work investigates the thermal conductivity of an FS3006-25 separator and commercial electrodes from two LIB cells. The first cell called Custom cell has an NMC cathode and a graphite anode. The other cell is type Melasta SLPBB042126; this cell has an LCO ($LiCoO_2$) cathode and a graphite anode. For detecting changes in thermal conductivity the materials are measured under different conditions and compaction pressure steps.

The separator thermal conductivity was found to be 0.116 ± 0.012 $Wk^{-1}m^{-1}$ at 2.7 bar applied pressure and showed increasing by 16 % when the pressure ranged from 2.7 to 11.6 bar. The thermal conductivity of the NMC cathode (fresh electrode) increased around 9 % from 0.35±0.05 to 0.38 ± 0.03 $Wk^{-1}m^{-1}$, while the LCO cathode (BOL electrode) ranged from 0.51±0.06 to 0.65 ± 0.14 $Wk^{-1}m^{-1}$ with 27 % increase. In the case of anodes, the pressure increased the Custom cell anode (fresh electrode) thermal conductivity with 40 % from 0.427 ± 0.008 to 0.597 ± 0.018 $Wk^{-1}m^{-1}$, while the Melasta anode showed the largest dependency on compaction pressure with 83 % increase from 0.6 ± 0.2 to 1.1 ± 0.4 $Wk^{-1}m^{-1}$.

Adding the electrolyte solvent to the measured samples increased the separator thermal conductivity by a factor of 3, while the NMC cathode (BOL electrode) increased by a factore of 2. The LCO cathode (BOL electrode) showed an increase of 3. Custom cell anode (BOL electrode) has the highest dependency on electrolyte solvent soaking where the thermal conductivity increased by a factor of 5, while the effect on the Melasta cell anode (BOL electrode) was a factor of about 2.

In addition, a simulation of the internal temperature distribution was done using both cells' measured conductivities and thicknesses. The models showed that adding the electrolyte to the cell layers decreases the centre temperature by 0.8 K for the Custom cell (30 A/m^2 charging current density), while the Mealata (13.1 A/m^2 charging current density) centre temperature decreased by 0.08 K.

Furthermore, the electrodes from a Custom cell battery at the beginning of life were extracted and the thermal conductivity measured and compared to fresh electrodes. The BOL battery cathode measurement showed around 35 % lower thermal conductivity values compared to the fresh cathode. In the case of the anode, the extracted materials physical structure conditions prevented the determination of the ageing impact on the thermal conductivity.

Finally, the thermal interface resistance between the LIB cell layers is measured. Results showed a thermal contact resistance of 4.3 ± 1.8 E-5 Km^2w^{-1} for the dry LCO cathode and 2.1 ± 0.8 E-5 Km^2w^{-1} for the NMC cathode. The Melasta cell anode thermal contact resistance is measured to be 6.5 ± 1.4 Km^2w^{-1}. Adding the electrolyte solvent decreased the thermal contact resistance by about 2 for the cathode and about 7 for the anode.

5.2 Further work

Some of the measurements showed a standard deviation that was as large as the thermal conductivity value itself. For more accuracy, the thermal conductivity measurements with significant stander deviation should be redone.

The original plan for this project was to open another Custom cell at the end of life phase to determine the impact of ageing on the thermal conductivity for the cell electrodes, but due to technical issues with the glovebox in the lab, that could not be done. Opening this cell and measure its components thermal conductivity will validate the effect of the battery ageing on the battery conductivity.

For the thermal contact resistance, investigate the effect of the SEI layer on the interface thermal resistance by measuring the extracted anodes without cleaning. That will give an understanding of the effect of this layer on the thermal behaviour of the cell.

Finally, the thermal model used in this project has many simplifications. Using more realistic thermal models that can simulate the temperature profiles for the battery will give more details about the effect of the thermal conductivity on the temperature distribution.

References

[1] Min-Kyu Song, Elton J Cairns, and Yuegang Zhang. "Lithium/sulfur batteries with high specific energy: old challenges and new opportunities". In: *Nanoscale* 5.6 (2013), pp. 2186–2204.

[2] Shriram Santhanagopalan et al. *Design and analysis of large lithium-ion battery systems*. Artech House, 2014.

[3] Pollet, Bruno Iain Staffell and Jin Lei Shang. *Current status of hybrid, battery and fuel cell electric vehicles From electrochemistry to market prospects*. URL: `https://www.sciencedirect.com/science/article/pii/S0013468612005671` (visited on 2012).

[4] Lena Spitthoff, Paul R Shearing, and Odne Stokke Burheim. "Temperature, Ageing and Thermal Management of Lithium-Ion Batteries". In: *Energies* 14.5 (2021), p. 1248. URL: `https://www.mdpi.com/1996-1073/14/5/1248`.

[5] Bandhauer T M Fuller T F and Garimella S. *A Critical Review of Thermal Issues in Lithium-Ion*. URL: `https://iopscience.iop.org/article/10.1149/1.3515880` (visited on 2011).

[6] Robert Bock et al. "Thermal gradients with sintered solid state electrolytes in lithium-ion batteries". In: *Energies* 13.1 (2020), p. 253.

[7] Frank Richter et al. "Thermal conductivity and internal temperature profiles of Li-ion secondary batteries". In: *Journal of Power Sources* 359 (2017), pp. 592–600. URL: `https://www.sciencedirect.com/science/article/pii/S037877531730678X`.

[8] Frank Richter et al. "Measurements of ageing and thermal conductivity in a secondary NMC-hard carbon Li-ion battery and the impact on internal temperature profiles". In: *Electrochimica Acta* 250 (2017), pp. 228–237. URL: `https://www.sciencedirect.com/science/article/pii/S0013468617316146`.

[9] SC Chen, CC Wan, and YY Wang. "Thermal analysis of lithium-ion batteries". In: *Journal of power sources* 140.1 (2005), pp. 111–124.

[10] Peyman Taheri and Majid Bahrami. "Temperature rise in prismatic polymer lithium-ion batteries: An analytic approach". In: *SAE International Journal of Passenger Cars-Electronic and Electrical Systems* 5.2012-01-0334 (2012), pp. 164–176.

[11] Odne Stokke Burheim. *Engineering energy storage*. Academic press, 2017.

[12] Yemeserach Mekonnen, Aditya Sundararajan, and Arif I Sarwat. "A review of cathode and anode materials for lithium-ion batteries". In: *SoutheastCon 2016*. IEEE. 2016, pp. 1–6.

[13] Walter van Schalkwijk and Bruno Scrosati. *Advances in lithium-ion batteries*. Springer Science & Business Media, 2007.

[14] Pallavi Verma, Pascal Maire, and Petr Novák. "A review of the features and analyses of the solid electrolyte interphase in Li-ion batteries". In: *Electrochimica Acta* 55.22 (2010), pp. 6332–6341.

[15] Naoki Nitta et al. "Li-ion battery materials: present and future". In: *Materials today* 18.5 (2015), pp. 252–264.

[16] Lars Ole Valøen and Jan N Reimers. "Transport properties of LiPF6-based Li-ion battery electrolytes". In: *Journal of The Electrochemical Society* 152.5 (2005), A882.

[17] R Byron Bird. "Transport phenomena". In: *Appl. Mech. Rev.* 55.1 (2002), R1–R4.

[18] Theodore L Bergman et al. *Fundamentals of heat and mass transfer*. John Wiley & Sons, 2011.

[19] O Burheim et al. “Ex situ measurements of through-plane thermal conductivities in a polymer electrolyte fuel cell”. In: *Journal of Power Sources* 195.1 (2010), pp. 249–256. URL: https://doi.org/10.1016/j.jpowsour.2009.06.077.

[20] Ximing Cheng et al. “Engineering-Oriented Modeling for Thermal Behaviors of 18650 Li-ion Batteries”. In: *Energy Procedia* 105 (2017), pp. 4757–4762.

[21] Van Mierlo G. Maggetto and Ph. Lataire. *Which Energy Source for Road Transport in the Future? A Comparison of Battery, Hybrid and Fuel Cell Vehicles.* URL: https://www.sciencedirect.com/science/article/pii/S0196890406000501 (visited on 2006).

[22] O. S. Burheim M. A. Onsrud P. J. S. Vie J. G. Pharoah and F. Vullum-Bruer. *Thermal conductivity, heat sources and temperature profiles of Li-ion batteries.* (Visited on 2014).

[23] Kinoshita and Dr Kim. Electrochemical. *Oxygen Technology.* (Visited on 1992).

[24] P. J. Osswald M. del Rosario J. Garche and A. Jossen. *Fast and accurate measurement of entropy profiles of commercial lithium-ion cells.* 2014. URL: https://www.sciencedirect.com/science/article/pii/S0013468615002376.

[25] Kristian Eggereide Roaldsnes. “Exploration of Nonlinearities in a Lithium Ion Battery Cell Model and their impact on Particle Filters and Nonlinear Kalman Filters for State of Charge Estimation”. MA thesis. NTNU, 2018.

[26] Christian Trandem. *Heat generation and cooling in lithium-ion pouch cells.* 2020.

[27] Viswanathan, Vilayanur Daiwon Choi Donghai Wang Silas Towne Jun Liu Ralph E. Williford Ji-Guang Zhang and Zhenguo Yang. *Effect of Entropy Change of Lithium Intercalation in Cathodes and Anodes on Li-Ion Battery Thermal Management.* URL: https://www.sciencedirect.com/science/article/pii/S0378775309021119 (visited on 2010).

[28] Gao Yang Jiuchun Jiang Caiping Zhang and Zeyu Ma. *Lithium-Ion Battery Aging Mechanisms and Life Model under Different Charging Stresses.* URL: https://www.sciencedirect.com/science/article/pii/S0378775317305876 (visited on 2017).

[29] F. Richter S. Kjelstrup O. Burheim and P. Vier. *Measurements of Ageing and Thermal Conductivity in a Secondary NMC-Hard Carbon Li-Ion Battery and the Impact on Internal Temperature Profiles.* URL: https://www.sciencedirect.com/science/article/pii/S0013468617316146 (visited on 2017).

[30] Daniel Sauerteig et al. “Reversible and irreversible dilation of lithium-ion battery electrodes investigated by in-situ dilatometry”. In: *Journal of Power Sources* 342 (2017), pp. 939–946.

A Appendix

Thermal resistance for the dry Custom cell anode material as a function of samples thickens.

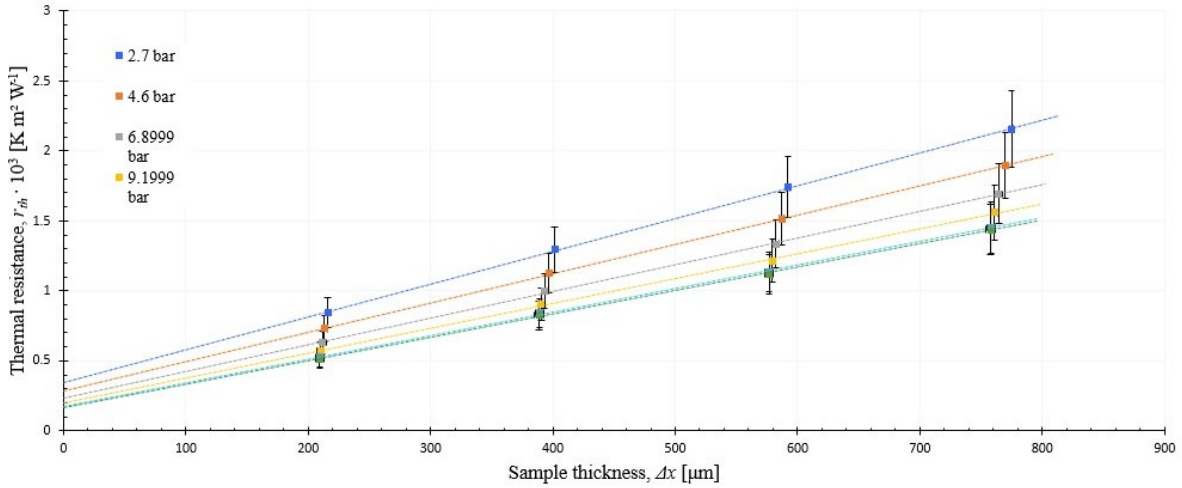

Figure A.1: Thermal resistance of Melasta cell dry anode as a function of s ample thickness

Tabell A.1: Measured thermal resistance for dry electrodes. (Km^2w^{-1}).

P[bar]	$R^{ML}_{cathode}$	R^{ML}_{anode}	$R^{CC}_{cathode}$	R^{CC}_{anode}
2.7	5.2 ± 0.6E-04	5.4 ± 0.6E-04	9.4 ± 1.0E-04	8.5 ± 1.0E-04
4.6	4.8 ± 0.6E-04	4.6 ± 0.5E-04	8.7 ± 1.0E-04	7.3 ± 0.9E-04
6.9	4.4 ± 0.5E-04	3.8 ± 0.4E-04	8.2 ± 1.0E-04	6.3 ± 0.7E-04
9.7	4.2 ± 0.5E-04	3.3 ± 0.4E-04	7.8 ± 0.9E-04	5.7 ± 0.7E-04
11.5	3.9 ± 0.4E-04	2.9 ± 0.3E-04	7.5 ± 0.9E-04	5.2 ± 0.6E-04
11.6	3.9 ± 0.4E-04	2.9 ± 0.3E-04	7.5 ± 0.9E-04	5.1 ± 0.6E-04

CC = Custom Cell

ML = Melasta Cell

Tabell A.2: Measured thermal resistance for FS6003-25 separator. Km^2w^{-1}.

P[bar]	$R^{dry}_{separator}$	$R^{wet}_{separator}$
2.7	(5.64 ±0.7)E-04	(1.9 ±0.2)E-04
4.6	(5.30 ±0.6)E-04	(1.8 ±0.2)E-04
6.9	(4.98 ±0.6)E-04	(1.8 ±0.2)E-04
9.7	(4.81 ±0.6)E-04	(1.8 ±0.2)E-04
11.5	(4.57 ±0.5)E-04	(1.8 ±0.2)E-04
11.6	(4.57 ±0.5)E-04	(1.9 ±0.2)E-04

Thermal conductivity for Custom and Melasta cells anodes (dry and wet) as a function of applied pressure.

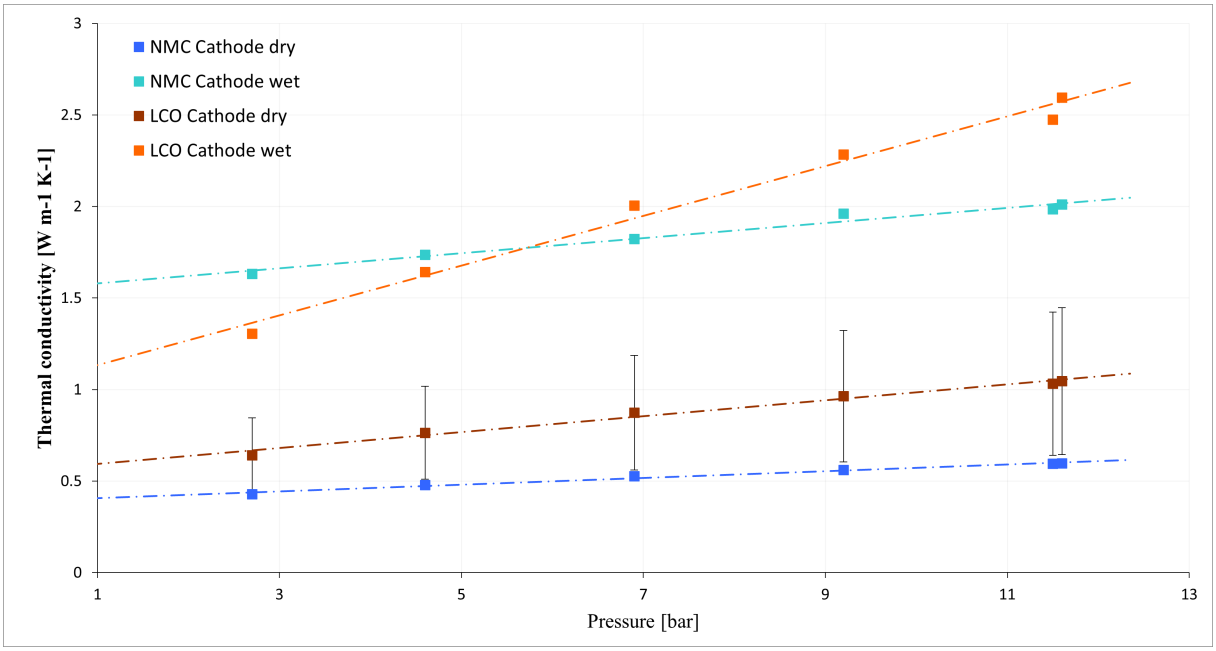

Figure A.2: Thermal conductivity for Custom and Melasta cells anodes (dry and wet) as a function of applied pressure.

1D temperature profile cross-plane an Custom and Melasta cells for dry and soaked in electrolyte solvent cell layers

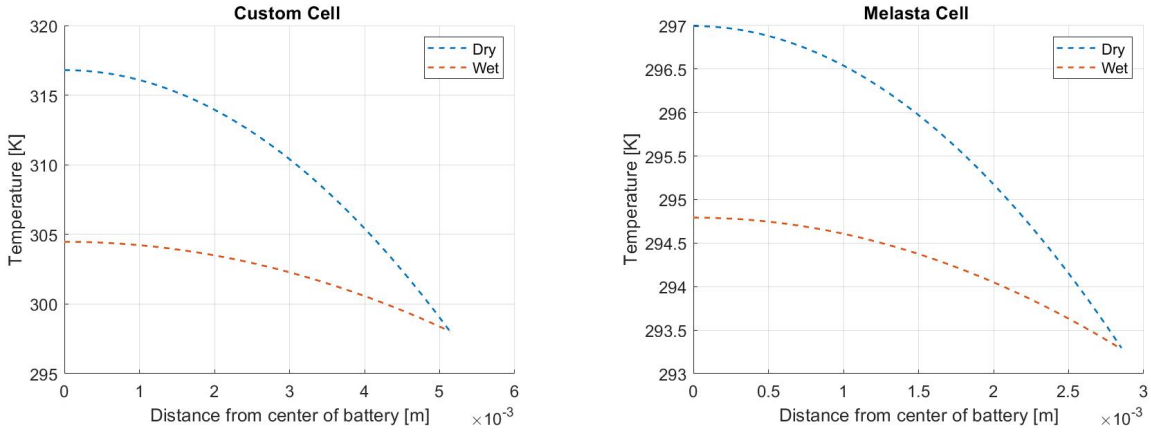

(a) Charging at 10 C-rate.

(b) Discharging at 10 C-rate.

Figure A.3: 1D temperature profile cross-plane an Custom and Melasta cells for dry and soaked in electrolyte solvent cell layers

Tabell A.3: Measured thermal conductivity values for the fresh and BOL custom cell dry electrodes. ($Wk^{-1}m^{-1}$).

P[bar]	$K_{cathode}^{BOL}$	$K_{cathode}^{fresh}$	K_{anode}^{BOL}	K_{anode}^{fresh}
2.7	0.47 ± 0.04	0.32 ± 0.04	0.39 ± 0.10	0.398 ± 0.008
4.6	0.49 ± 0.04	0.32 ± 0.03	0.54 ± 0.15	0.445 ± 0.006
6.9	0.51 ± 0.04	0.33 ± 0.03	0.7 ± 0.2	0.489 ± 0.016
9.2	0.53 ± 0.04	0.34 ± 0.03	0.9 ± 0.3	0.52 ± 0.02
11.5	0.53 ± 0.04	0.34 ± 0.03	1.0 ± 0.4	0.553 ± 0.019
11.6	0.54 ± 0.04	0.34 ± 0.03	1.2 ± 0.5	0.554 ± 0.017

B Appendix

Table showing the measured thermal conductivities of the Melasta cell stacked samples.

Tabell B.1: Measured effective thermal conductivity of Melasta A-S and C-S

P[bar]	K^{dry}_{A-S} $(Wk^{-1}m^{-1})$	K^{wet}_{A-S} $(Wk^{-1}m^{-1})$	K^{dry}_{C-S} $(Wk^{-1}m^{-1})$	K^{wet}_{C-S} $(Wk^{-1}m^{-1})$
2.7	0.35 ± 0.13	1.0 ± 0.8	0.32 ± 0.03	0.82 ± 0.05
4.6	0.39 ± 0.13	1.0 ± 0.9	0.34 ± 0.02	0.82 ± 0.05
6.9	0.39 ± 0.11	1.1 ± 0.9	0.34 ± 0.03	0.83 ± 0.03
9.2	0.40 ± 0.10	1.1 ± 0.9	0.35 ± 0.04	0.87 ± 0.02
11.5	0.41 ± 0.10	1.0 ± 1.0	0.36 ± 0.03	0.90 ± 0.03
11.6	0.41 ± 0.10	1.2 ± 0.9	0.36 ± 0.02	0.92 ± 0.06

Table showing the calculated thermal conductivities of the Melasta cell stacked samples.

Tabell B.2: Calculated effective thermal conductivity of Melasta A-S and C-S

P[bar]	K^{dry}_{A-S} $(Wk^{-1}m^{-1})$	K^{wet}_{A-S} $(Wk^{-1}m^{-1})$	K^{dry}_{C-S} $(Wk^{-1}m^{-1})$	K^{wet}_{C-S} $(Wk^{-1}m^{-1})$
2.7	0.27 ± 0.02	0.94 ± 0.17	0.32 ± 0.03	0.81 ± 0.12
4.6	0.28 ± 0.02	1.04 ± 0.19	0.34 ± 0.02	0.83 ± 0.13
6.9	0.29 ± 0.03	1.14 ± 0.17	0.34 ± 0.04	0.87 ± 0.12
9.7	0.31 ± 0.03	1.21 ± 0.19	0.35 ± 0.03	0.92 ± 0.13
11.5	0.32 ± 0.03	1.3 ± 0.2	0.36 ± 0.03	0.95 ± 0.14
11.6	0.32 ± 0.03	1.3 ± 0.3	0.36 ± 0.02	0.9 ± 0.2

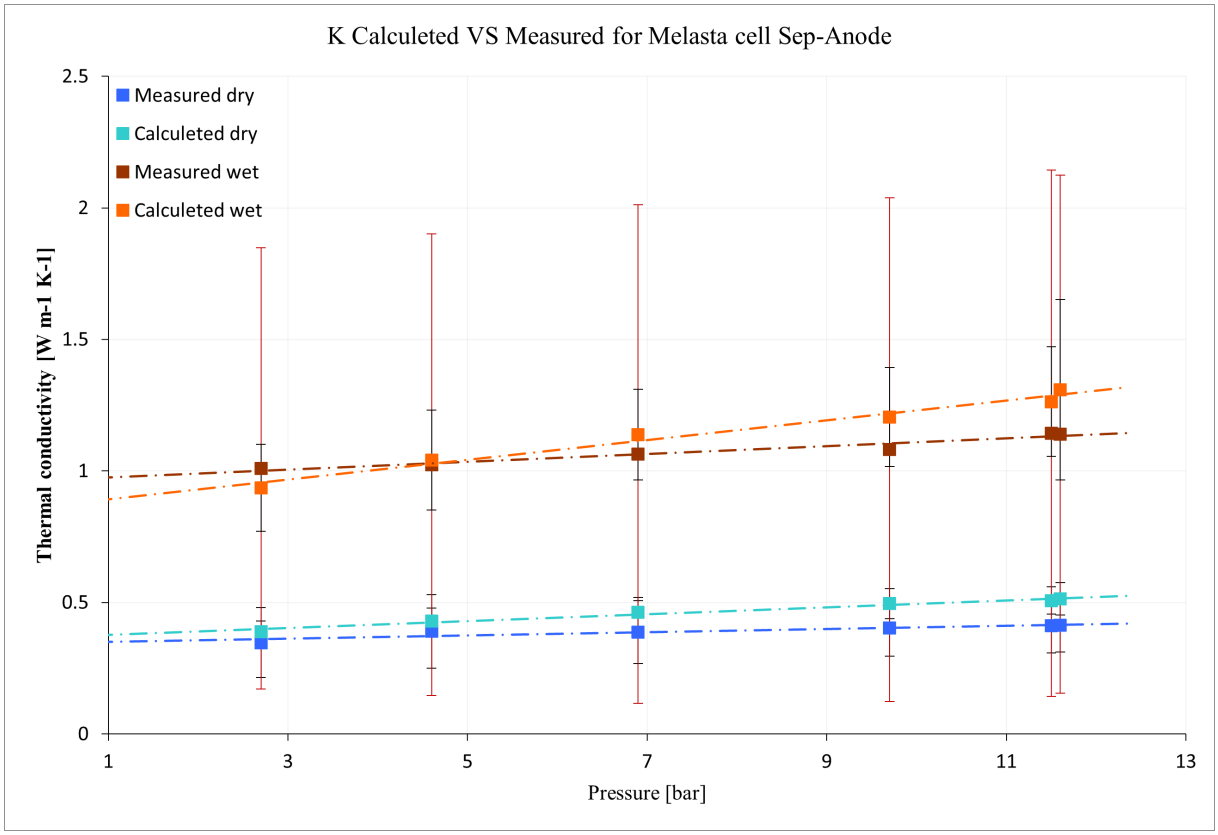

Figure B.1: Thermal conductivity of the separator - cathode (dry) as a function of applied pressure

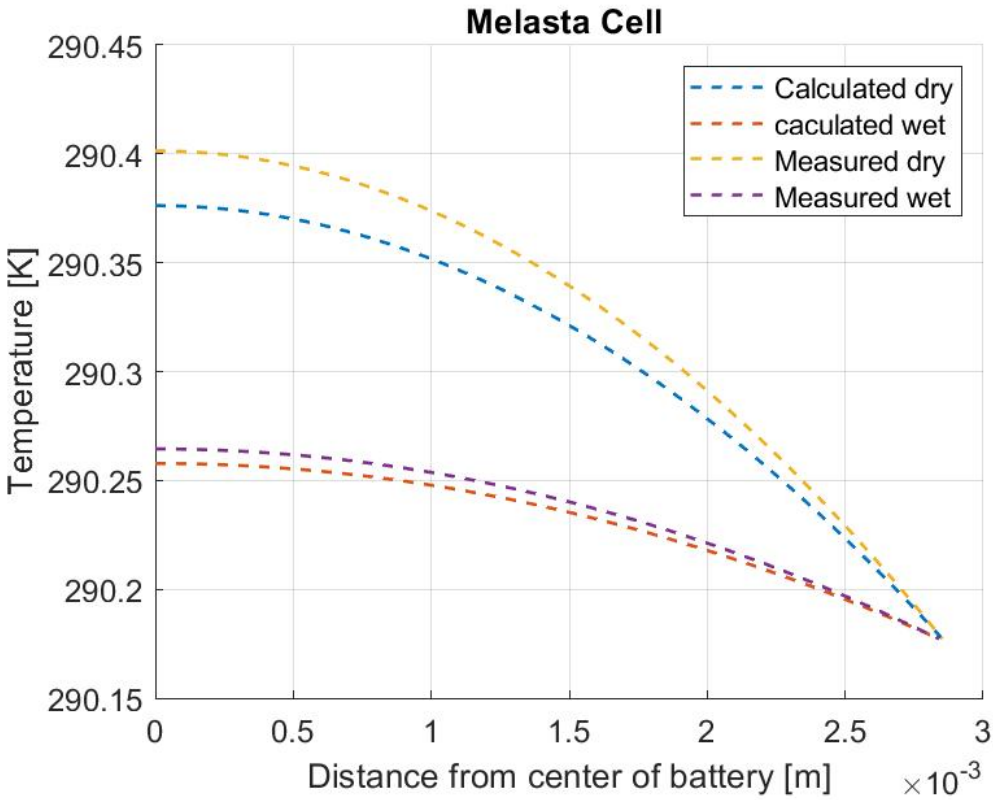

Figure B.2: Temperature distribution in the Melasta cell during discharge including the thermal interface resistance effect on the effective thermal conductivity.

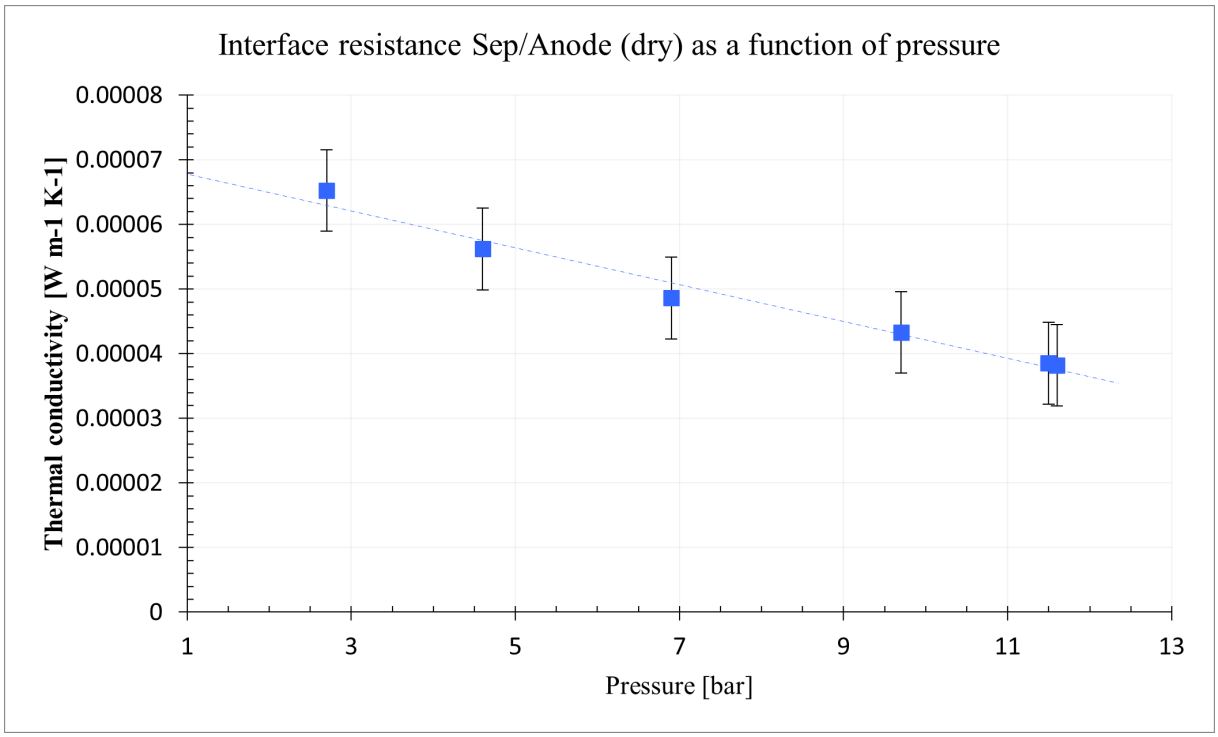

Figure B.3: Contact resistance between separator- anode (dry) as a function of pressure

C Appendix

1. 序言 PREFACE

此规格书适用于深圳市风云电池有限公司的锂聚合物可充电电池产品

The specification is suitable for the performance of Lithium-Polymer (LIP) rechargeable battery produced by the SHENZHEN MELASTA BATTERY CO., LTD.

2. 型号 MODEL

SLPBB042126HN 6550mAh 10C 3.7V

3. 产品规格 SPECIFICATION

单颗电池规格 Specifications of single cell

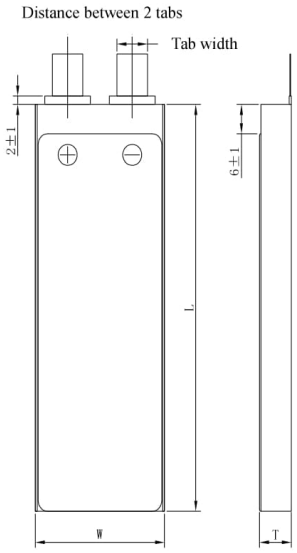

◆电芯正极材料 Cell Cathode Material		LiCoO2
◆标称容量 Typical Capacity①		6550mAh
◆标称电压 Nominal Voltage		3.7V
◆ 充电条件 Charge Condition	最大电流 Max. Continuous charge Current	13.1A
	峰值充电 Peak charge current	64A(≤0.5sec) 54A(≤1sec)
	电压 Voltage	4.2V±0.03V
◆ 放电条件 Discharge Condition	Max Continuous Discharge Current	65.5A
	Peak Discharge Current	98.25A(≤3sec)
	Cut-off Voltage	3.0V
◆交流内阻 AC Impedance(mOHM)		<3.0
◆循环寿命【充电:1C,放电:10C】 Cycle Life【CHA:1C,DCH:10C】		>100cycles
◆使用温度 Operating Temp.	充电 Charge	0℃~60℃
	放电 Discharge	-20℃~70℃
◆ 电芯尺寸 Cell Dimensions	厚度 Thickness(T)	10.7±0.3mm
	宽度 Width(W)	42±0.5mm
	长度 Length(L)	127.5±0.5mm
	极耳间距 Distance between 2 tabs	21±1mm
◆ 极耳尺寸 Dimensions of Cell tabs	极耳材料 Tab Material	Nickel-plated Copper
	极耳宽度 Tab Width	12mm
	极耳厚度 Tab Thickness	0.2mm
	极耳长度 Tab Length	30±1.5mm
◆重量 Weight(g)		128.5±3.0g
①标称容量：0.2C,4.2V~3.0V@23℃±2℃ Typical Capacity:0.2C,4.2V~3.0V@23℃±2℃		

Figure C.1: Melasta cell data sheet